


 Cite this: *RSC Adv.*, 2025, 15, 26515

# First-principles investigation and photovoltaic assessment of Cs<sub>2</sub>SnZ<sub>6</sub> (Z = Cl, Br, I) lead-free perovskites for future solar technologies

 Md. Ferdous Rahman,<sup>ID</sup>\*<sup>a</sup> Abu Saiyed,<sup>a</sup> Md. Faruk Hossain,<sup>b</sup> Latha Marasamy,<sup>ID</sup><sup>c</sup> Tanvir Al Galib,<sup>a</sup> Mahabur Rahman<sup>a</sup> and Mutasem Z. Bani-Fwaz<sup>d</sup>

This study presents a comprehensive first-principles and device-level investigation into the structural, electronic, optical, and photovoltaic properties of vacancy-ordered lead-free perovskites Cs<sub>2</sub>SnZ<sub>6</sub> (Z = Cl, Br, I) for next-generation solar energy conversion. Using density functional theory (DFT), we examined the structural stability, band structure, density of states, and optical response of Cs<sub>2</sub>SnCl<sub>6</sub>, Cs<sub>2</sub>SnBr<sub>6</sub>, and Cs<sub>2</sub>SnI<sub>6</sub>. The calculated direct bandgaps are 2.652 eV for Cs<sub>2</sub>SnCl<sub>6</sub>, 1.358 eV for Cs<sub>2</sub>SnBr<sub>6</sub>, and 0.228 eV for Cs<sub>2</sub>SnI<sub>6</sub>, demonstrating significant tunability through halide substitution. Optical analyses reveal strong absorption in the visible spectrum, with a redshift in absorption onset from Cl to I, enhancing light-harvesting capabilities. To assess device performance, SCAPS-1D simulations were employed with four different electron transport layers (ETLs): CdS, IGZO, SnS<sub>2</sub>, and ZnS. The Cs<sub>2</sub>SnBr<sub>6</sub>-based PSC with IGZO ETL achieved the highest power conversion efficiency (PCE) of 26.22%, driven by optimal band alignment and balanced charge transport. Meanwhile, Cs<sub>2</sub>SnI<sub>6</sub>, despite exhibiting ultrahigh short-circuit current densities ( $J_{SC} > 70 \text{ mA cm}^{-2}$ ) due to its narrow bandgap, showed poor performance with ZnS ETL due to mismatched energy levels. These results highlight the potential of Cs<sub>2</sub>SnZ<sub>6</sub> perovskites as promising lead-free absorber materials and emphasize the critical role of ETL compatibility and absorber optimization in achieving high-efficiency solar cells.

Received 17th May 2025

Accepted 19th July 2025

DOI: 10.1039/d5ra03487f

[rsc.li/rsc-advances](http://rsc.li/rsc-advances)

## 1. Introduction

The quest for clean, renewable, and sustainable energy sources has become an urgent global imperative amidst rising environmental concerns, climate change, and the pressing need to decarbonize the global energy economy.<sup>1,2</sup> Among the diverse range of renewable energy systems, photovoltaic (PV) solar energy stands at the forefront due to its abundance, scalability, and minimal environmental impact. Silicon (Si) has emerged as the predominant material for commercial solar cell applications owing to its favorable properties, including stability, high power conversion efficiency (PCE), and resistance to radiation.<sup>3</sup> The development of conventional solar cells, particularly those based on silicon (Si), has been limited by inherent drawbacks, including silicon's indirect and suboptimal bandgap, as well as the high costs associated with its fabrication processes.<sup>4</sup> In

recent decades, halide perovskite solar cells (PSCs) have garnered extraordinary interest owing to their rapid rise in PCE, reaching over 26% within a decade, along with their low-cost processing and tunable optoelectronic properties.<sup>5–13</sup> However, the commercialization of perovskite-based PV devices remains hindered by issues of toxicity, primarily due to the inclusion of lead (Pb), and long-term material instability under operational conditions.<sup>14,15</sup> This has stimulated intensive research into the discovery and optimization of lead-free perovskite alternatives that combine environmental benignity with high photovoltaic performance. Although extensive efforts have been devoted to developing lead-free perovskite materials, attaining PCE and environmental stability on par with their lead-based counterparts remains a significant challenge.<sup>16,17</sup> Therefore, there is a pressing demand within the photovoltaic (PV) sector to explore lead-free, high-efficiency materials that are viable for large-scale commercial deployment.<sup>18</sup>

A promising class of lead-free perovskites under exploration is based on vacancy-ordered double perovskite structures of the form A<sub>2</sub>BIVZ<sub>6</sub>, where A is a monovalent cation (e.g., Cs<sup>+</sup>), BIV is a group-IV metal such as Sn<sup>4+</sup>, and Z is a halide anion (Cl<sup>-</sup>, Br<sup>-</sup>, I<sup>-</sup>).<sup>19</sup> Among these, cesium tin halide perovskites, Cs<sub>2</sub>SnZ<sub>6</sub> (Z = Cl, Br, I), have emerged as compelling candidates due to their favorable structural stability, moderate direct bandgaps, and nontoxic nature.<sup>20</sup> Moreover, Cs<sub>2</sub>SnZ<sub>6</sub> exhibits a high-symmetry

<sup>a</sup>Advanced Energy Materials and Solar Cell Research Laboratory, Department of Electrical and Electronic Engineering, Begum Rokeya University, Rangpur 5400, Bangladesh. E-mail: ferdousapee@gmail.com

<sup>b</sup>Department of Physics, Rajshahi University of Engineering & Technology, Rajshahi, 6204, Bangladesh

<sup>c</sup>Facultad de Química, Materiales-Energía, Universidad Autónoma de Querétaro, Santiago de Querétaro, Querétaro, C.P.76010, Mexico

<sup>d</sup>Department of Chemistry, College of Science, King Khalid University, P. O. Box 9004, Abha 61413, Saudi Arabia



arrangement in the  $Fm\bar{3}m$  space group, similar to the structure of cubic halide perovskites.<sup>21–23</sup> Notably, the vacancy-ordered  $\text{Cs}_2\text{SnZ}_6$  compounds differ fundamentally from their  $\text{Sn}^{2+}$ -based counterparts (e.g.,  $\text{CsSnZ}_3$ ), offering enhanced resistance to oxidation and improved ambient stability, which is a pivotal factor in ensuring long-term device performance.<sup>24,25</sup> Despite these advantages, their practical photovoltaic potential remains underexplored, particularly in relation to their interfacial alignment with charge transport layers, which plays a crucial role in governing charge separation and extraction dynamics in solar cell architectures.

Recent simulation-based investigations on lead-free double perovskites such as  $\text{Cs}_2\text{AgBiBr}_6$  and  $\text{Cs}_2\text{SnI}_6$  have demonstrated promising optoelectronic performance and environmental stability, making them suitable candidates for photovoltaic applications.<sup>26–28</sup> For instance,  $\text{Cs}_2\text{AgBiBr}_6$  has shown respectable PCE values in numerical models under optimized conditions,<sup>26</sup> while  $\text{Cs}_2\text{SnI}_6$  exhibits favorable bandgap alignment and defect tolerance as validated by SCAPS-1D and DFT studies.<sup>28</sup> These studies highlight the potential of vacancy-ordered and mixed-halide perovskites, motivating the exploration of alternative Sn-based compositions such as  $\text{Cs}_2\text{SnZ}_6$ .

First-principles density functional theory (FP-DFT) calculations offer a robust platform for probing the intrinsic material properties of perovskites at the atomic scale, enabling insights into electronic band structure, optical absorption characteristics, effective masses, and defect tolerance. When complemented with device-level simulations, such as those conducted using SCAPS-1D software, a comprehensive evaluation of the photovoltaic behavior of these materials can be achieved. This dual-level approach allows for the rational selection of compatible electron transport layers (ETLs) that are critical for optimizing band alignment, minimizing recombination losses, and enhancing overall device efficiency. In this context, CdS, IGZO (indium gallium zinc oxide),  $\text{SnS}_2$ , and ZnS have been identified as promising ETLs due to their appropriate bandgaps, high electron mobility, and chemical compatibility with various perovskites.<sup>29–31</sup>

In this study, we present a comprehensive theoretical and numerical investigation into the structural, electronic, and optical properties of  $\text{Cs}_2\text{SnZ}_6$  compounds using first-principles density functional theory. We systematically evaluate their suitability as absorber materials in lead-free PSCs, focusing on bandgap tunability, absorption coefficients, dielectric response, and charge transport properties. Subsequently, we assess the photovoltaic performance of  $\text{Cs}_2\text{SnZ}_6$ -based solar cells using SCAPS-1D simulations, incorporating four different ETLs: CdS, IGZO,  $\text{SnS}_2$ , and ZnS. Through detailed energy band alignment analysis and performance metrics including open-circuit voltage ( $V_{\text{OC}}$ ), short-circuit current density ( $J_{\text{SC}}$ ), fill factor (FF), and overall PCE, we identify the optimal material configurations for enhanced device performance. This integrative approach provides valuable insights into the interfacial and device-level phenomena that govern the operation of lead-free perovskite solar cells, offering a strategic pathway for the development of stable, efficient, and environmentally benign photovoltaic technologies.

Our findings underscore the immense potential of  $\text{Cs}_2\text{SnZ}_6$  halides as next-generation photovoltaic absorbers and demonstrate the critical influence of ETL selection on the efficiency and stability of the resulting devices. The implications of this work extend beyond material discovery to encompass device engineering strategies that can accelerate the deployment of lead-free perovskite photovoltaics in real-world applications.

## 2. Simulation methodology with DFT and SCAPS-1D

The structural and electronic properties of  $\text{Cs}_2\text{SnZ}_6$  compounds were thoroughly investigated using an integrated computational methodology that combines advanced theoretical tools. Specifically, first-principles density functional theory (DFT) calculations<sup>32</sup> were carried out to gain deep insights into the behavior of these materials at the atomic level. The simulations employed on-the-fly generated (OTFG) ultrasoft pseudopotentials,<sup>33,34</sup> which are well-suited for achieving high accuracy in modeling complex materials systems. Additionally, the Perdew–Burke–Ernzerhof (PBE) exchange–correlation functional, within the generalized gradient approximation (GGA) framework,<sup>35</sup> was used to describe electron interactions. This approach enabled precise evaluation of the ground-state electronic structure, bonding nature, and stability of  $\text{Cs}_2\text{SnZ}_6$  compounds, leveraging the robust predictive power of DFT.<sup>33</sup>

The computational protocol incorporated essential input parameters such as lattice constants, Brillouin zone sampling grids, crystal structure data, and kinetic energy cut-off values. These parameters were judiciously selected to ensure reliable and precise simulation outcomes within the DFT framework.<sup>18,36,37</sup> To enhance the accuracy of structural optimizations and electronic property evaluations, a kinetic energy cut-off of 750 eV was employed for all  $\text{Cs}_2\text{SnZ}_6$  configurations.<sup>38</sup>

For self-consistent field (SCF) calculations, the energy convergence criterion was set to  $10^{-6}$  atomic units, with the highest force threshold of  $0.01 \text{ eV } \text{Å}^{-1}$  is ensured accurate ground-state energy determinations. During structural relaxation and ionic optimization, a force convergence limit of  $10^{-4}$  atomic units was applied. Band structure and partial density of states (PDOS) calculations utilized a Monkhorst–Pack  $k$ -point mesh of  $10 \times 10 \times 10$  to achieve high-resolution sampling of the Brillouin zone.<sup>39</sup>

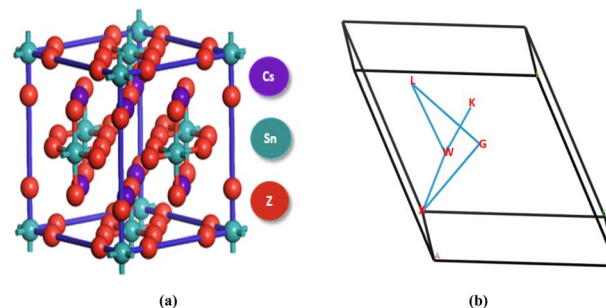


Fig. 1 (a) Crystal structure of  $\text{Cs}_2\text{SnZ}_6$  compound, and (b) the initial Brillouin zone (BZ)  $k$ -vector trajectory.



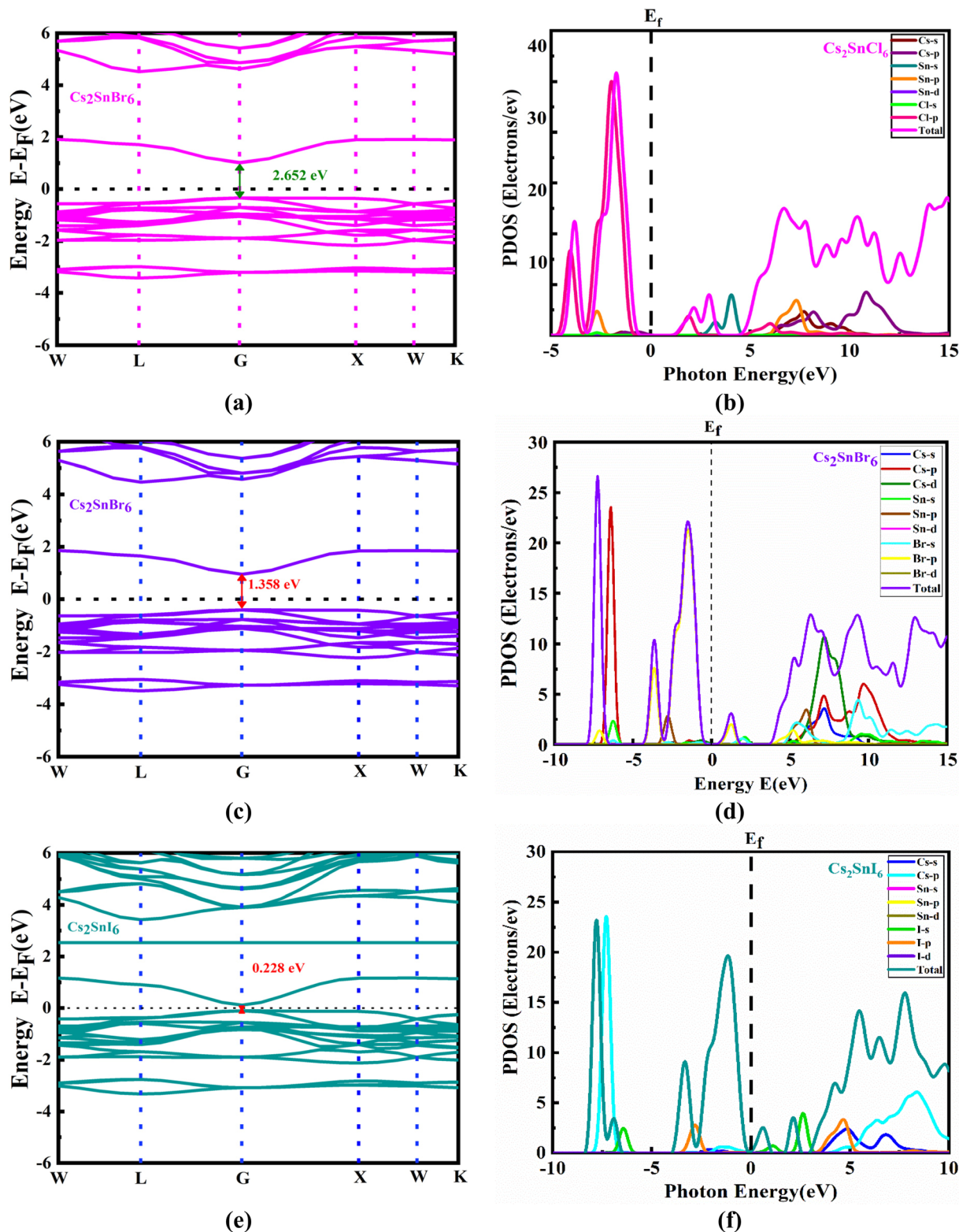


Fig. 2 (a) Electronic band structure and (b) PDOS of  $\text{Cs}_2\text{SnCl}_6$ , (c) electronic band structure and (d) PDOS of  $\text{Cs}_2\text{SnBr}_6$ , and (e) electronic band structure and (f) PDOS of  $\text{Cs}_2\text{SnI}_6$ .

The optical properties of the materials were investigated through first-order time-dependent perturbation theory, which enabled the analysis of dynamic structural stability and

optoelectronic response. In particular, the frequency-dependent complex dielectric function,  $\epsilon(\omega) = \epsilon_1(\omega) + j\epsilon_2(\omega)$ , was computed to elucidate the interaction between incident photons and the

**Table 1** The variation of lattice constant, unit-cell volume, and direct energy bandgap of  $\text{Cs}_2\text{SnZ}_6$  in GGA-PBE function

Material	Lattice constant (Å)	Bandgap (eV)	Unit-cell volume (a.u.) <sup>3</sup>
$\text{Cs}_2\text{SnCl}_6$	10.49	2.652 (GGA-PBE)	1155.34
$\text{Cs}_2\text{SnBr}_6$	10.99	1.358 (GGA-PBE)	1326.03
$\text{Cs}_2\text{SnI}_6$	11.78	0.228 (GGA-PBE)	1634.48

material system. This function facilitated the determination of optical absorption coefficients across a broad photon energy spectrum (in electron volts, eV), providing insight into light-matter interactions and energy harvesting potential. For these calculations, a Gamma-centered  $10 \times 10 \times 10$  Monkhorst-Pack  $k$ -mesh was adopted to maintain consistency with structural and electronic evaluations.

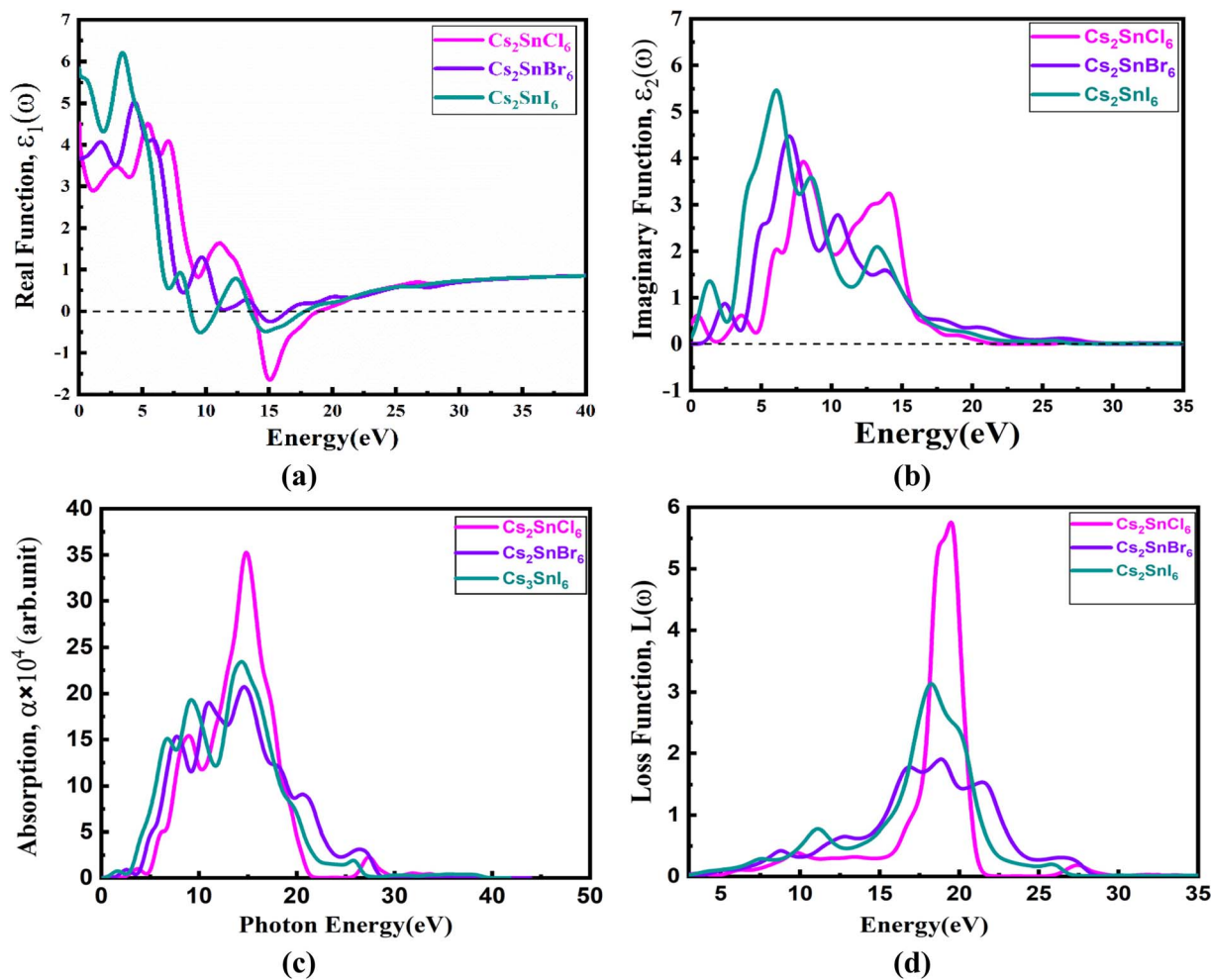


**Fig. 3** The energy-dependent (a) dielectric real function, (b) dielectric imaginary function, (c) absorption index, and (d) loss function.

**Table 2** Utilized data sources for the device structure simulation

Parameters (units)	FTO <sup>64</sup>	IGZO <sup>65</sup>	SnS <sub>2</sub> (ref. 66)	CdS <sup>67</sup>	ZnS <sup>68</sup>	$\text{Cs}_2\text{SnCl}_6$	$\text{Cs}_2\text{SnBr}_6$	$\text{Cs}_2\text{SnI}_6$
Thickness (nm)	50	50	50	50	50	1000	1000	1000
Bandgap (eV)	3.6	3.050	2.24	2.40	2.80	1.652	1.358	0.228
Electron affinity (eV)	4	4.160	4.24	4.20	3.80	3.620	4.250	4.642
Dielectric permittivity	9	10	10	10	9	4.520	3.660	5.750
CB effective DOS (cm <sup>-3</sup> )	$2.2 \times 10^{18}$	$5 \times 10^{18}$	$2.2 \times 10^{18}$	$2.8 \times 10^{19}$	$2.2 \times 10^{18}$	$1.89 \times 10^{17}$	$1.890 \times 10^{17}$	$1.848 \times 10^{17}$
VB effective DOS (cm <sup>-3</sup> )	$1.8 \times 10^{19}$	$5 \times 10^{18}$	$1.8 \times 10^{19}$	$2.8 \times 10^{19}$	$1.8 \times 10^{19}$	$1.629 \times 10^{18}$	$1.392 \times 10^{18}$	$1.258 \times 10^{18}$
Electron mobility (cm <sup>2</sup> V <sup>-1</sup> s <sup>-1</sup> )	100	15	50	100	100	25	25	30
Hole mobility (cm <sup>2</sup> V <sup>-1</sup> s <sup>-1</sup> )	25	10	50	25	25	20	25	30
Donor density, ND (cm <sup>-3</sup> )	$5 \times 10^{18}$	$1 \times 10^{18}$	$1 \times 10^{17}$	$1 \times 10^{18}$	$1 \times 10^{17}$	0	0	0
Acceptor density, NA (cm <sup>-3</sup> )	0	0	0	0	0	$1 \times 10^{17}$	$1 \times 10^{17}$	$1 \times 10^{17}$
Bulk defect density, Nt (cm <sup>-3</sup> )	$10^{14}$	$1 \times 10^{15}$	$1 \times 10^{14}$	$10^{14}$	$10^{14}$	$10^{12}$	$10^{12}$	$10^{12}$



To simulate device-level performance, the one-dimensional Solar Cell Capacitance Simulator (SCAPS-1D), developed by the Department of Electronics and Information Systems (ELIS) at Ghent University, Belgium, was employed. The simulated photovoltaic device structure comprised Al/FTO/ETL/ $\text{Cs}_2\text{SnZ}_6$ /Au layers. Through this framework, the electrical behavior of the heterojunction was modeled by solving the coupled

continuity equations for electrons and holes, as well as the Poisson equation under equilibrium conditions. The simulations rigorously assessed carrier transport dynamics and energy band alignment, enabling a comprehensive evaluation of the photovoltaic potential of  $\text{Cs}_2\text{SnZ}_6$ -based lead-free perovskite solar cells.<sup>40,41</sup>

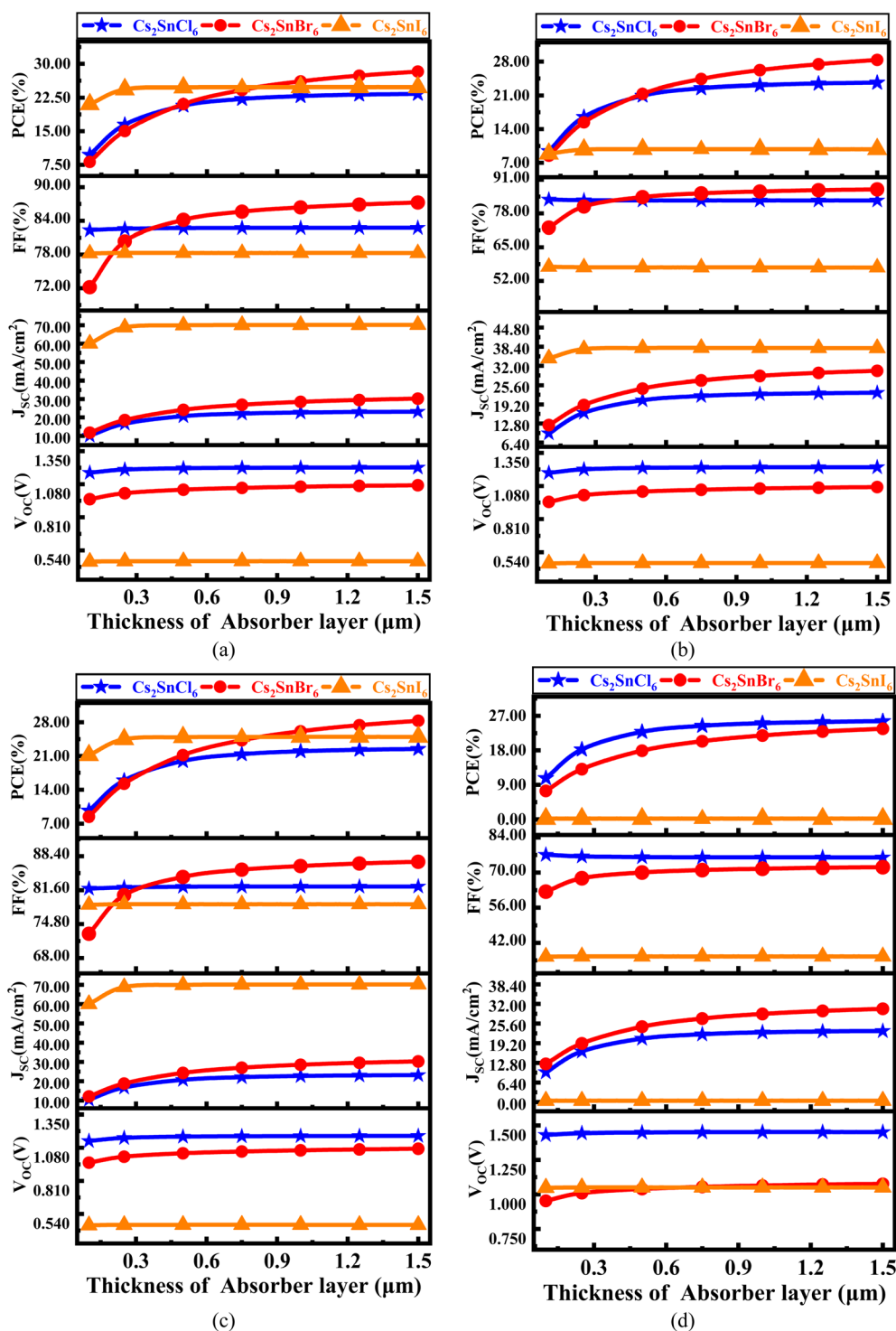


Fig. 4 Thickness dependent PV parameters for different  $\text{Cs}_2\text{SnZ}_6$  absorber layer with (a) CdS, (b) IGZO, (c)  $\text{SnS}_2$ , and (d) ZnS ETL.



### 3. Result and discussion

#### 3.1 DFT-based investigation of new inorganic cubic perovskites $\text{Cs}_2\text{SnZ}_6$

**3.1.1 Structural properties.**  $\text{Cs}_2\text{SnZ}_6$  is a well-defined inorganic halide compound crystallizing in the cubic  $Fm\bar{3}m$  space group with space group number 225.<sup>19,42,43</sup> Structurally, it

comprises cesium (Cs) as the monovalent cation and a combination of tetravalent tin (Sn) and halide anions (Cl, Br, or I), forming a highly symmetric cubic lattice. The unit cell of  $\text{Cs}_2\text{SnZ}_6$  consists of nine atoms, with Cs, Sn, and Z atoms occupying distinct Wyckoff positions. Specifically, the halide atom Z (Cl/Br/I) is located at fractional coordinates (0.25, 0.25, 0.75), while the four Sn atoms are symmetrically positioned at

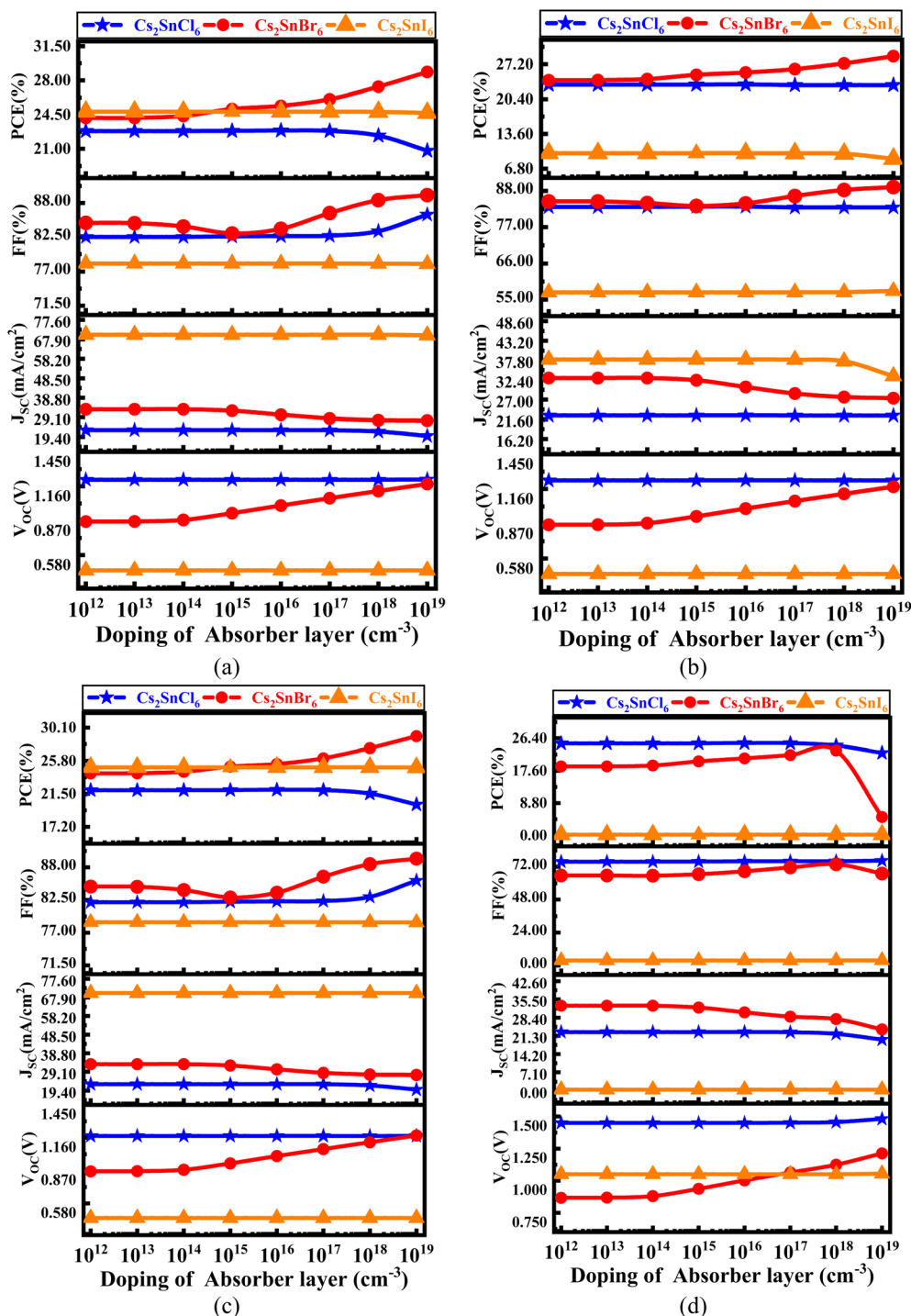


Fig. 5 Variation in PV parameters with different doping concentrations having various  $\text{Cs}_2\text{SnZ}_6$  absorber layers for (a) CdS, (b) IGZO, (c)  $\text{SnS}_2$ , and (d) ZnS ETL.



(0, 0, 0). The corresponding halide atoms, such as Br in the case of  $\text{Cs}_2\text{SnBr}_6$ , occupy positions at (0, 0.5, 0.75). This atomic arrangement is visually represented in Fig. 1(a), which depicts the precise crystallographic configuration.

Fig. 1(b) illustrates the high-symmetry path of the  $k$ -vector within the first Brillouin zone (BZ), which is essential for evaluating the electronic band structure. The calculated band structures of  $\text{Cs}_2\text{SnZ}_6$  compounds are significantly governed by transitions near the high-symmetry points W, L, G, X, and W. These points critically determine the electronic dispersion and the overall shape of the band diagram. Using first-principles computational techniques, the optimized lattice constants were determined to be approximately 10.49 Å for  $\text{Cs}_2\text{SnCl}_6$ , 10.99 Å for  $\text{Cs}_2\text{SnBr}_6$ , and 11.78 Å for  $\text{Cs}_2\text{SnI}_6$ , indicating a systematic lattice expansion with increasing halide ionic radius.

**3.1.2 Electronic properties.** The electronic band structures of the inorganic cubic substance  $\text{Cs}_2\text{SnZ}_6$  were computed to improve our comprehension of its optical and electronic properties. Fig. 2(a–c) illustrates the electronic band structures of the  $\text{Cs}_2\text{SnZ}_6$  framework. Fig. 2 presents the electronic band structures of  $\text{Cs}_2\text{SnZ}_6$ , with the Fermi level aligned at zero to facilitate

accurate determination of the bandgap. The reciprocal space trajectory traced along the high-symmetry points W–L–G–X–W is employed to characterize the band dispersion within the cubic Brillouin zone. For all three compounds— $\text{Cs}_2\text{SnCl}_6$ ,  $\text{Cs}_2\text{SnBr}_6$ , and  $\text{Cs}_2\text{SnI}_6$ —both the valence band maximum (VBM) and conduction band minimum (CBM) are located at the  $\Gamma$  point, indicating a direct bandgap nature, as clearly illustrated in Fig. 2. The G point represents the center of the Brillouin zone, while W, L, and X denote critical high-symmetry points that define the key electronic transitions in the crystal momentum space.

The calculated direct bandgaps using the generalized gradient approximation (GGA-PBE) exchange–correlation functional are 2.652 eV for  $\text{Cs}_2\text{SnCl}_6$ , 1.358 eV for  $\text{Cs}_2\text{SnBr}_6$ , and 0.228 eV for  $\text{Cs}_2\text{SnI}_6$ . These values reveal a clear trend of bandgap narrowing with increasing halide ionic radius, which can be attributed to the decreasing electronegativity and enhanced orbital overlap in larger halide anions. As the electronegativity of the halide decreases from Cl to I, the bonding nature becomes increasingly ionic to covalent, which enhances the overlap between the halide p-orbitals and the Sn-5p orbitals. This increased orbital overlap results in stronger antibonding

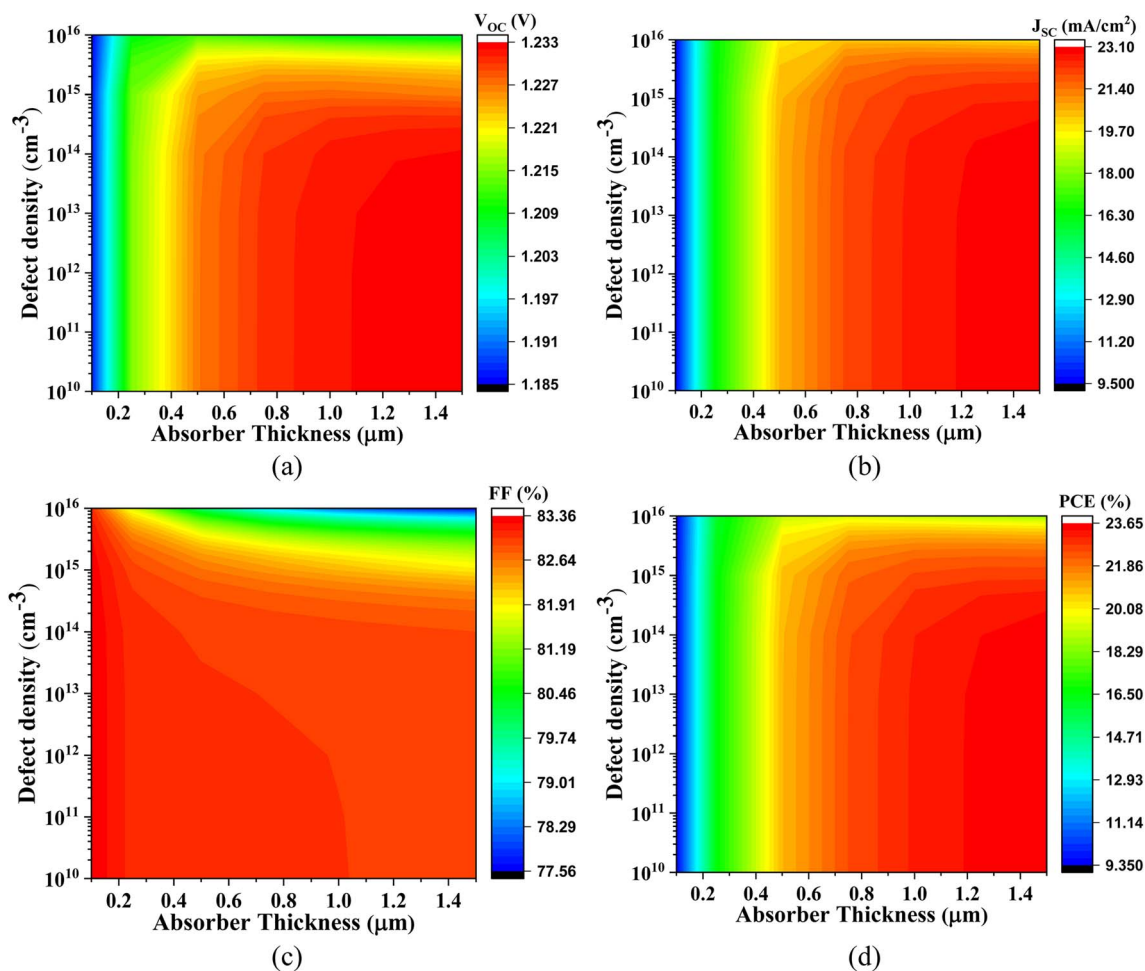


Fig. 6 Simultaneous influence of absorber thickness and defect density on the output of  $\text{Cs}_2\text{SnCl}_6$ -based PSC with IGZO ETL, (a)  $V_{oc}$ , (b)  $J_{sc}$ , (c) FF, and (d) PCE.



interactions at the VBM and CBM, leading to a reduction in the bandgap energy.<sup>23,44</sup> Additionally, larger halide ions (like  $\text{I}^-$ ) cause lattice expansion, which reduces the crystal field splitting and further narrows the bandgap.<sup>23</sup> This trend is explicitly presented in Table 1, highlighting the influence of halide substitution on electronic structure. The relatively wide bandgap of  $\text{Cs}_2\text{SnCl}_6$  contrasts with the narrower gaps of  $\text{Cs}_2\text{SnBr}_6$  and  $\text{Cs}_2\text{SnI}_6$ , underscoring the tunability of these materials for specific optoelectronic applications. Notably, the presence of a direct bandgap makes these compounds particularly suitable for photovoltaic and optoelectronic devices, where efficient photon absorption and electron–hole generation are essential.<sup>44–46</sup> The distinct band gaps and Fermi level positioned near the valence band (VB), along with a higher density of states in the VB than in the conduction band (CB), confirm the p-type semiconducting nature of these materials.<sup>47</sup>

To elucidate the influence of various atomic species and their corresponding electronic states on the bandgap characteristics of  $\text{Cs}_2\text{SnZ}_6$  compounds, we performed detailed Partial Density of States (PDOS) calculations. This analysis was aimed at achieving a deeper understanding of how specific atomic orbitals contribute to the formation and modulation of the

electronic bandgap. As illustrated in Fig. 2(b), (d) and (f), the PDOS profiles span the energy range from  $-10$  eV to  $+10$  eV, highlighting the energy distribution and orbital contributions of Cs, Sn, and halide atoms to the electronic structure of the compounds. The PDOS results reveal significant orbital hybridization between the electronic states of cesium (Cs) and the halide ions ( $\text{Cl}^-$ ,  $\text{Br}^-$ ,  $\text{I}^-$ ) with tin (Sn), which is sustained across a wide energy interval. This hybridization coexists with the preservation of a finite bandgap, confirming the semi-conducting nature of these compounds. A prominent observation is the weak involvement of Cs electronic states near the Fermi level; Cs orbitals reside far from the conduction and VB edges, and therefore, their direct contribution to the band-edge states is minimal. Additionally, electron density transfer from Cs atoms to Sn and halide atoms suggests notable charge redistribution within the lattice.

For all  $\text{Cs}_2\text{SnZ}_6$  compounds, the VBM is primarily governed by antibonding interactions involving Sn-5p and halogen-p orbitals, while the CBM arises mainly from Sn-5p and Cs-5d antibonding orbitals, as depicted in Fig. 2. In the valence region, the Br-p orbitals dominate across all compounds, while additional contributions are observed from Cs-p and Cl-s

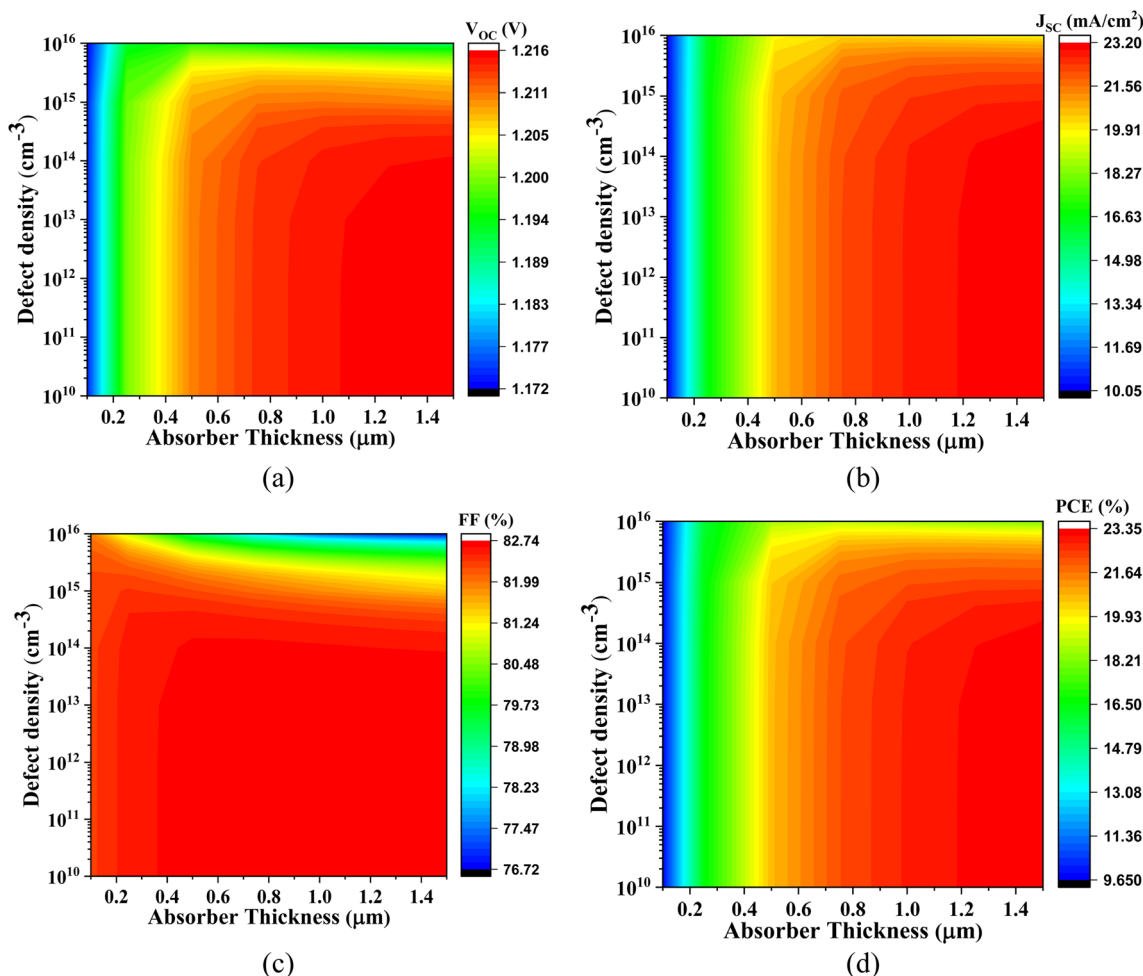


Fig. 7 Impact of active layer thickness and defect density of  $\text{Cs}_2\text{SnCl}_6$ -based PSC with CdS ETL on (a)  $V_{OC}$ , (b)  $J_{SC}$ , (c) FF, and (d) PCE.



orbitals in  $\text{Cs}_2\text{SnCl}_6$ , Cs-p, Sn-d, and Br-d orbitals in  $\text{Cs}_2\text{SnBr}_6$ , and Cs-p, Sn-d, and I-d orbitals in  $\text{Cs}_2\text{SnI}_6$ , respectively. The substitution of halide anions introduces notable variations in both the PDOS and the Total Density of States (TDOS), as reflected in the PDOS curves. Distinct shifts in the peak intensities of the TDOS are observed across the three compounds, with maximum values measured at 35.85 for  $\text{Cs}_2\text{SnCl}_6$ , 26.60 for  $\text{Cs}_2\text{SnBr}_6$ , and 23.42 for  $\text{Cs}_2\text{SnI}_6$ , respectively. These disparities underscore the pronounced impact of halide substitution on the electronic structure, altering the density and distribution of states across the energy spectrum. The observed modifications in the TDOS highlight the unique electronic fingerprints of each compound and affirm the role of Z-anion engineering in tuning the optoelectronic properties of  $\text{Cs}_2\text{SnZ}_6$  perovskites for photovoltaic applications.

**3.1.3 Optical properties.** Analyzing the optical properties of materials is a fundamental step in determining their suitability for optoelectronic and photovoltaic applications. Such analyses typically involve evaluating key optical parameters, including the real and imaginary parts of the dielectric function, optical absorption spectrum, and the electron energy loss function (ELF). The frequency-dependent complex dielectric function,

represented as  $\varepsilon(\omega)$ , characterizes a material's response to incident electromagnetic radiation and reflects its complex permittivity. This function is composed of two primary components: the real part,  $\varepsilon_1(\omega)$ , which corresponds to the dispersion of the electromagnetic wave, and the imaginary part,  $\varepsilon_2(\omega)$ , which represents the absorption of energy from the field. These relationships are formally expressed as:

$$\varepsilon(\omega) = \varepsilon_1(\omega) + i\varepsilon_2(\omega) \quad (1)$$

The  $\varepsilon_1(\omega)$  is computed through the application of the Kramers-Kronig transformation, a fundamental mathematical technique that derives  $\varepsilon_1(\omega)$  from the frequency-dependent behavior of the  $\varepsilon_2(\omega)$ .<sup>47–52</sup> This transformation establishes a causal relationship between the two components of the complex dielectric function. In contrast, the  $\varepsilon_2(\omega)$  is determined based on the momentum matrix elements, which quantify electronic transitions between occupied and unoccupied states under photon excitation.<sup>49,50,54,55</sup> Furthermore, essential optical parameters such as the absorption coefficient ( $\alpha$ ) and the electron energy loss function (ELF) can be directly extracted from the real and imaginary parts of the dielectric function.<sup>53</sup> These properties are pivotal in assessing a material's interaction with

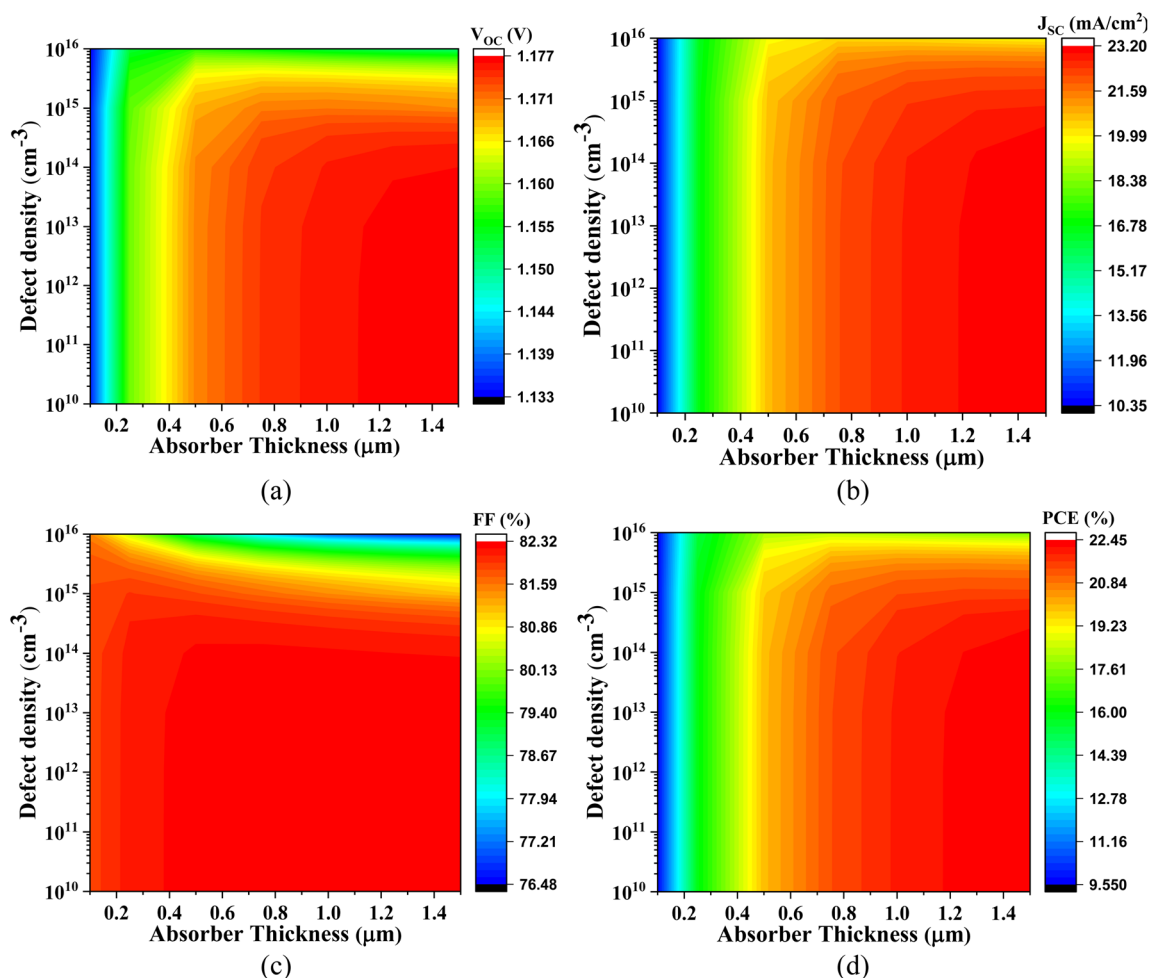


Fig. 8 Effect of absorber layer thickness and defect density on (a)  $V_{OC}$ , (b)  $J_{SC}$ , (c) FF, and (d) PCE of  $\text{Cs}_2\text{SnCl}_6$ -based PSC with  $\text{SnS}_2$  ETL.



electromagnetic radiation and its potential efficacy in optoelectronic applications.<sup>48–50,56</sup>

The expression for the real component of the dielectric function, denoted as  $\varepsilon_1(\omega)$ , can be formulated as follows:<sup>56,57</sup>

$$\varepsilon_1(\omega) = 1 + \frac{2}{\pi} P \int_0^{\infty} \frac{\varepsilon_2(\omega') \omega'}{(\omega'^2 - \omega^2)} d\omega' \quad (2)$$

Here,  $P$  represents the integral prime value.

The mathematical expression for the  $\varepsilon_2(\omega)$ , in terms of the momentum operator, can be formally represented as follows:<sup>56,57</sup>

$$\varepsilon_2(\omega) = \frac{V e^2}{2\pi \hbar m^2 \omega^2} \times \int d^3 k \sum |\langle \phi_c | p | \phi_v \rangle|^2 \delta(E_c - E_v - \hbar\omega) \quad (3)$$

In this formulation,  $V$  denotes the volume of the unit cell,  $\hbar$  represents the reduced Planck constant, and  $p$  corresponds to the momentum operator. The symbols  $\phi_c$  and  $\phi_v$  refer to the wave functions of the VB and CB, respectively, while  $E_c$  and  $E_v$  indicate the energy levels of the CB and VB. Additionally,  $\delta$  represents the Dirac delta function, which enforces energy conservation during electronic transitions. Utilizing both the real component  $\varepsilon_1(\omega)$  and the imaginary component  $\varepsilon_2(\omega)$  of the

complex dielectric function, the optical absorption coefficient  $\alpha$  can be evaluated using the following relation:<sup>56,57</sup>

$$\alpha(\omega) = \frac{\sqrt{2}\omega}{c} \left[ \sqrt{\varepsilon_1(\omega)^2 - \varepsilon_2(\omega)^2} - \varepsilon_1(\omega) \right]^{1/2} \quad (4)$$

In this expression,  $\omega$  denotes the angular frequency of the incident electromagnetic radiation, while  $c$  refers to the speed of light in a vacuum. Finally, the electron energy loss function (ELF), which characterizes the energy dissipated by fast electrons traversing the material, can be computed using the following relation:<sup>48,56</sup>

$$L(\omega) = \frac{\varepsilon_2(\omega)}{\varepsilon_1(\omega)^2 - \varepsilon_2(\omega)^2} \quad (5)$$

**3.1.3.1 Real function.** Fig. 3(a) presents the real part of the dielectric function,  $\varepsilon_1(\omega)$ , for  $\text{Cs}_2\text{SnZ}_6$  compounds across a photon energy range extending up to 7 eV. The real component,  $\varepsilon_1(\omega)$ , reflects the material's polarizability and dispersive behavior in response to an externally applied electric field, offering critical insight into its dielectric screening and refractive characteristics.<sup>52,58</sup> Each compound shows a positive  $\varepsilon_1(\omega)$  within the 0–5 eV energy range, which is characteristic of

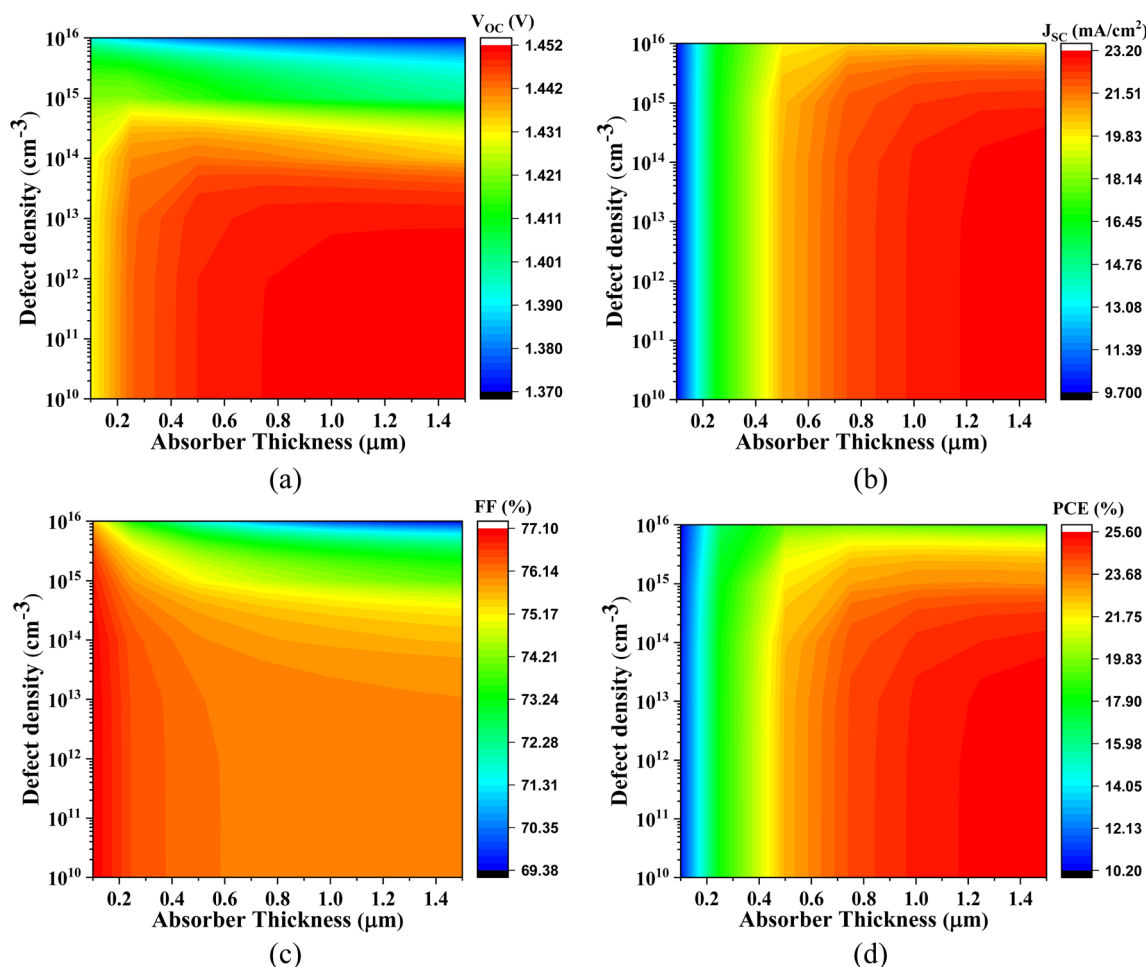


Fig. 9 Role of the active layer thickness and defect density on (a)  $V_{OC}$ , (b)  $J_{SC}$ , (c) FF, and (d) PCE of  $\text{Cs}_2\text{SnCl}_6$ -based PSC with CdS ETL.



semiconducting materials.<sup>59</sup> The parameter  $\epsilon_1(0)$ , representing the static dielectric constant or the electronic contribution at zero frequency, plays a pivotal role in characterizing a material's intrinsic optical response and is directly obtained from the real part of the dielectric function,  $\epsilon_1(\omega)$ . For the cubic perovskite compounds  $\text{Cs}_2\text{SnCl}_6$ ,  $\text{Cs}_2\text{SnBr}_6$ , and  $\text{Cs}_2\text{SnI}_6$ , the calculated  $\epsilon_1(0)$  values are 4.51, 3.66, and 5.83, respectively. The lowest  $\epsilon_1(0)$  observed for  $\text{K}_2\text{InSbBr}_6$  among the halide series can be attributed to the bandgap–dielectric relationship described by the Penn model, where reduced electronic polarizability leads to lower dielectric response in materials with wider bandgaps.<sup>60</sup> Although  $\text{K}_2\text{InSbBr}_6$  does not exhibit the largest bandgap, its lower density of electronic states near the band edges and less effective orbital overlap—compared to the F and I analogs—result in diminished dielectric screening and reduced  $\epsilon_1(0)$ . Distinctive trends are observed in the spectral behavior of  $\epsilon_1(\omega)$  when these materials are subjected to incident optical radiation. The real dielectric component initially increases from its static value, reaching a peak at specific photon energies, and subsequently undergoes a sharp decline. This characteristic response indicates a strong dielectric polarization within a limited energy range, reflecting the material's capability to interact efficiently with electromagnetic radiation.

Generally, materials with larger bandgaps tend to exhibit lower peak values in their dielectric functions due to reduced electronic polarizability, whereas those with narrower bandgaps show stronger optical responses. As the halide anion in  $\text{Cs}_2\text{SnZ}_6$  is varied from Cl to I, a noticeable blueshift in the dielectric function is observed, wherein the  $\epsilon_1(\omega)$  peak shifts toward higher photon energies. This shift is attributed to the increase in bandgap energy, which modifies the onset of interband transitions and alters the material's optical dispersion characteristics. Conversely, as the halogen size increases, the peak intensity rises, likely due to the enhanced polarizability associated with bigger halogen atoms.<sup>61</sup>

**3.1.3.2 Imaginary function.** Fig. 3(b) depicts the spectral behavior of the  $\epsilon_2(\omega)$ , for  $\text{Cs}_2\text{SnZ}_6$  compounds with halide substitutions. The  $\epsilon_2(\omega)$  provides critical insights into the electronic bandgap characteristics and the material's optical absorption properties, as it directly reflects the interband electronic transitions induced by incident photons.<sup>5</sup> It is intricately associated with the material's band structure in the previous studies.<sup>58</sup> The values of  $\epsilon_2(\omega)$  for  $\text{Cs}_2\text{SnZ}_6$  materials exhibit a wide absorption spectrum, reflecting their diverse absorption capabilities. As shown in Fig. 3(b), the  $\epsilon_2(\omega)$  peaks for  $\text{Cs}_2\text{SnCl}_6$ ,  $\text{Cs}_2\text{SnBr}_6$ , and  $\text{Cs}_2\text{SnI}_6$  are observed at optical energies of 3.92,

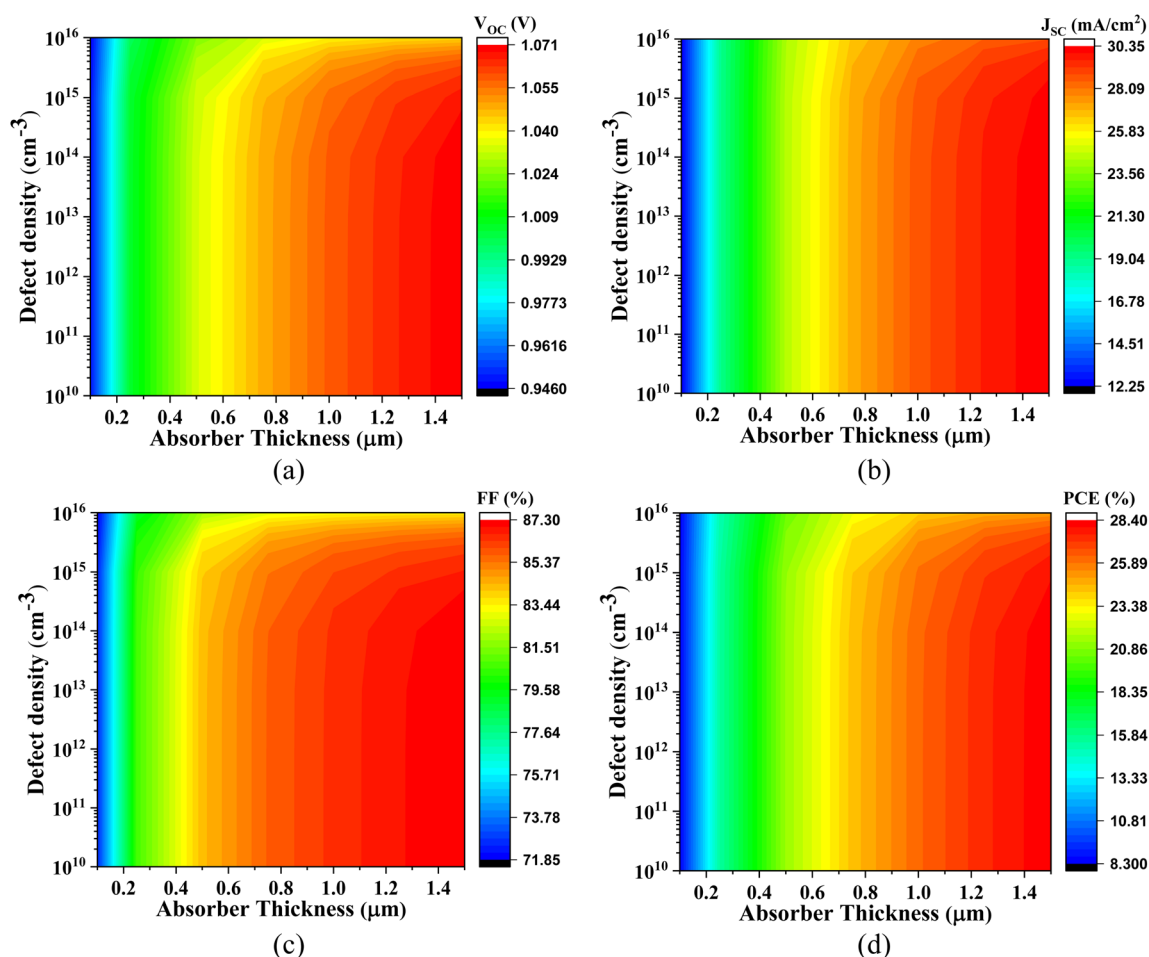


Fig. 10 Impact of absorber thickness and defect density on (a)  $V_{\text{OC}}$ , (b)  $J_{\text{SC}}$ , (c) FF, and (d) PCE of  $\text{Cs}_2\text{SnBr}_6$ -based PSC with IGZO ETL.



4.47, and 5.46 eV, corresponding to photon absorption energies of 7.98 eV, 6.98 eV, and 6.07 eV, respectively. These peaks in the imaginary component of the dielectric constant align with the transitions of carriers from the VB to the CB. The peak positions vary due to changes in the composition of the Z-anions. Notably, the spectra reveal a consistent trend where the peaks shift toward lower values as the size of the Z-anions increases from Cl to I in the  $\text{Cs}_2\text{SnZ}_6$  structures. Furthermore, the materials under study exhibit an imaginary dielectric constant approaching zero at photon energies above 35 eV, indicating excellent optical transparency and minimal light absorption.

**3.1.3.3 Absorption coefficients.** The optical absorption coefficient is crucial for understanding a material's ability to absorb and convert light energy into other forms, such as heat or electrical energy, making it essential for solar cell applications.<sup>58,62</sup> Fig. 3(c) illustrates the relationship between the absorption coefficient and photon energy for  $\text{Cs}_2\text{SnZ}_6$  structures. In the context of solar cell applications, the primary absorption peak is particularly significant, as it indicates the wavelength range where a material can efficiently absorb electromagnetic radiation. The initial peak determines whether the  $\text{Cs}_2\text{SnZ}_6$  structures can absorb within the visible light spectrum. Among the optical absorption spectra of all the materials, the most prominent peak is observed in the visible region.

The observed changes in absorption within  $\text{Cs}_2\text{SnZ}_6$  closely correspond to the expected bandgap of the materials. In the visible spectrum, the absorption coefficient for  $\text{Cs}_2\text{SnZ}_6$  increases as the size of the Z-anions grows, which is a desirable characteristic for solar cell applications. As the Z-anions transition from Cl to I, the material's bandgap decreases, resulting in a redshift of the absorption edge toward the lower energy region. Of the four materials,  $\text{Cs}_2\text{SnCl}_6$  exhibits the highest absorption coefficient at 14.78 eV.

**3.1.3.4 Energy loss function (ELF).** The ELF quantifies the energy dissipation of electrons as they travel through a dielectric medium. The  $L(\omega)$  representation of the ELF is valuable for examining a material's response to light. Fig. 3(d) shows that the ELF peaks for  $\text{Cs}_2\text{SnZ}_6$ , with a cubic structure, occur within the energy range of 15 to 22 eV. The relatively low magnitude of  $L(\omega)$  in the visible region for the studied materials indicates that these halide compounds possess strong light absorption capabilities.<sup>63</sup> The peaks in the ELF diagrams of  $\text{Cs}_2\text{SnZ}_6$  correspond to energy dissipation that takes place when the energy of the incident photon exceeds the material's bandgap. It is clear that when the photon energy does not surpass the bandgap, no significant scattering occurs. Prominent peaks were observed at different energy levels for the  $\text{Cs}_2\text{SnCl}_6$ ,  $\text{Cs}_2\text{SnBr}_6$ , and  $\text{Cs}_2\text{SnI}_6$  compounds, specifically at 19.45 eV, 18.88 eV, and 18.31 eV,

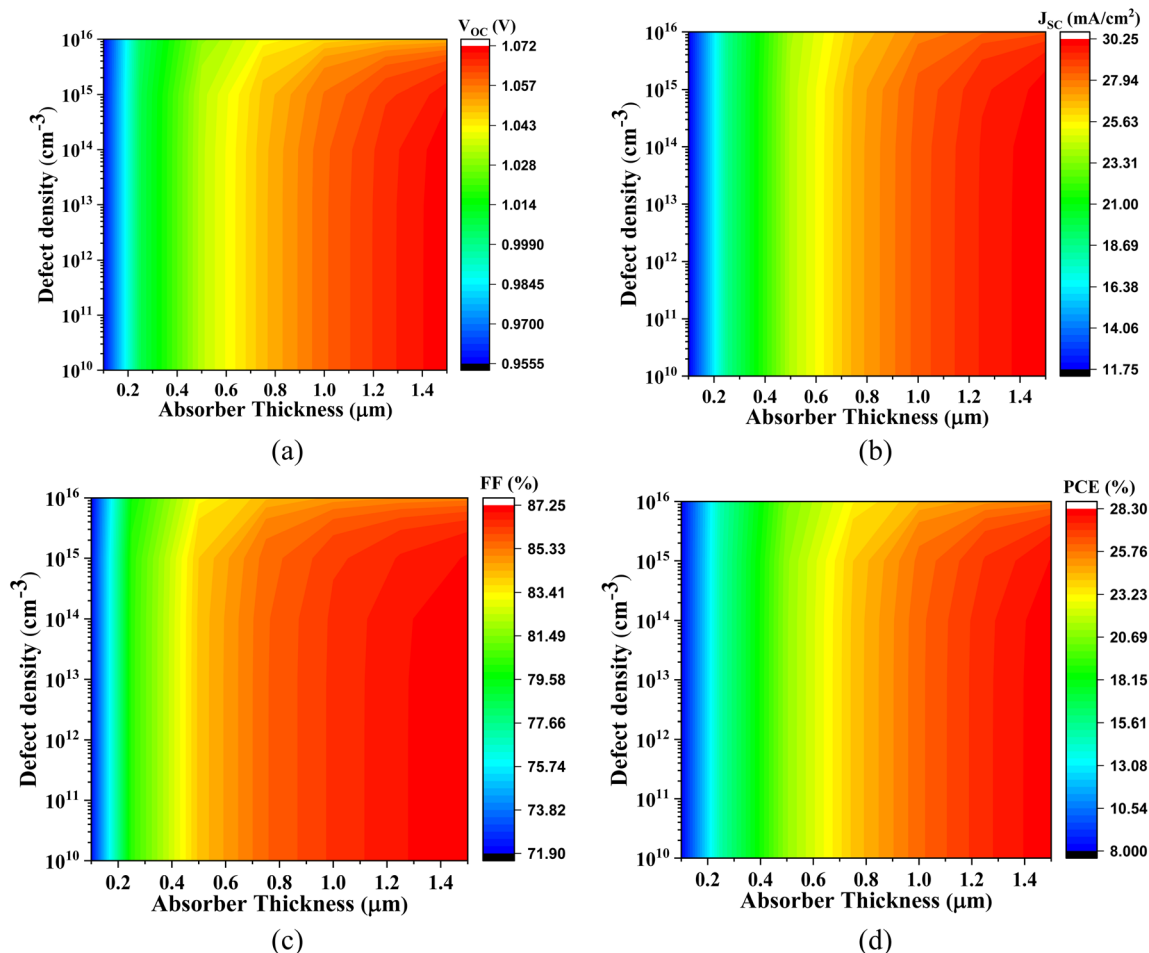


Fig. 11 Impact of active layer thickness and defect density on (a)  $V_{OC}$ , (b)  $J_{SC}$ , (c) FF, and (d) PCE of  $\text{Cs}_2\text{SnBr}_6$ -based PSC with CdS ETL.



respectively. Across all configurations, it is evident that as the size of the Z-anions increases, the optical loss shifts toward lower photon energies, commonly referred to as a redshift. Among the four materials, Fig. 3(d) demonstrates that  $\text{Cs}_2\text{SnCl}_6$  exhibits the greatest energy loss.

### 3.2 SCAPS-1D simulation analysis

Table 2 presents the optimized PV parameters corresponding to absorber thicknesses 1000 nm for each ETL configuration.

#### 3.2.1 Optimization of the thickness of the absorber layer.

Fig. 4 comprehensively illustrates the impact of varying the absorber layer thickness from 0  $\mu\text{m}$  to 1.5  $\mu\text{m}$  on the performance optimization of the simulated lead-free perovskite-inspired PV devices.

In Fig. 4(a), the effect of absorber thickness on device performance using CdS as the ETL is analyzed. The variation in thickness directly alters the built-in electric field strength and modulates the charge separation and transport dynamics. The  $V_{\text{OC}}$  for  $\text{Cs}_2\text{SnCl}_6$  increases from 1.174 V to 1.216 V, and for  $\text{Cs}_2\text{SnBr}_6$ , from 0.957 V to 1.070 V. These enhancements are primarily attributed to improved charge carrier extraction and reduced interfacial recombination. In contrast,  $\text{Cs}_2\text{SnI}_6$  displays a relatively stable  $V_{\text{OC}}$ , suggesting that this parameter is less

sensitive to thickness-induced changes in the internal electric field for this specific absorber. The  $J_{\text{SC}}$  increases markedly from 11.72 to 23.18  $\text{mA cm}^{-2}$  for  $\text{Cs}_2\text{SnCl}_6$  and from 11.76 to 30.24  $\text{mA cm}^{-2}$  for  $\text{Cs}_2\text{SnBr}_6$ . These improvements reflect increased photon absorption and enhanced photogenerated carrier collection.  $\text{Cs}_2\text{SnI}_6$  maintains a consistently high  $J_{\text{SC}}$ , which is characteristic of its narrow bandgap and high intrinsic absorption coefficient.

At absorber thicknesses  $\geq 1000$  nm, a saturation effect in spectral absorption is evident, accompanied by a rise in recombination losses, particularly for devices with lower mobility ETLs. This behavior aligns with previous experimental and theoretical studies. The FF exhibits a linear upward trend for  $\text{Cs}_2\text{SnCl}_6$  and  $\text{Cs}_2\text{SnI}_6$ , indicating improved diode quality and lower series resistance. For  $\text{Cs}_2\text{SnBr}_6$ , the FF rises significantly from 72.17% to 87.24%, pointing to superior charge transport properties at increased thicknesses. Consequently, the PCE demonstrates a substantial improvement across all absorber types with increased thickness. Specifically, the PCE is increased from 9.76% to 23.32% for  $\text{Cs}_2\text{SnCl}_6$ , from 8.12% to 28.26% for  $\text{Cs}_2\text{SnBr}_6$ , and from 21.01% to 24.80% for  $\text{Cs}_2\text{SnI}_6$ , affirming the beneficial role of optimized thickness in enhancing photon management and charge collection.

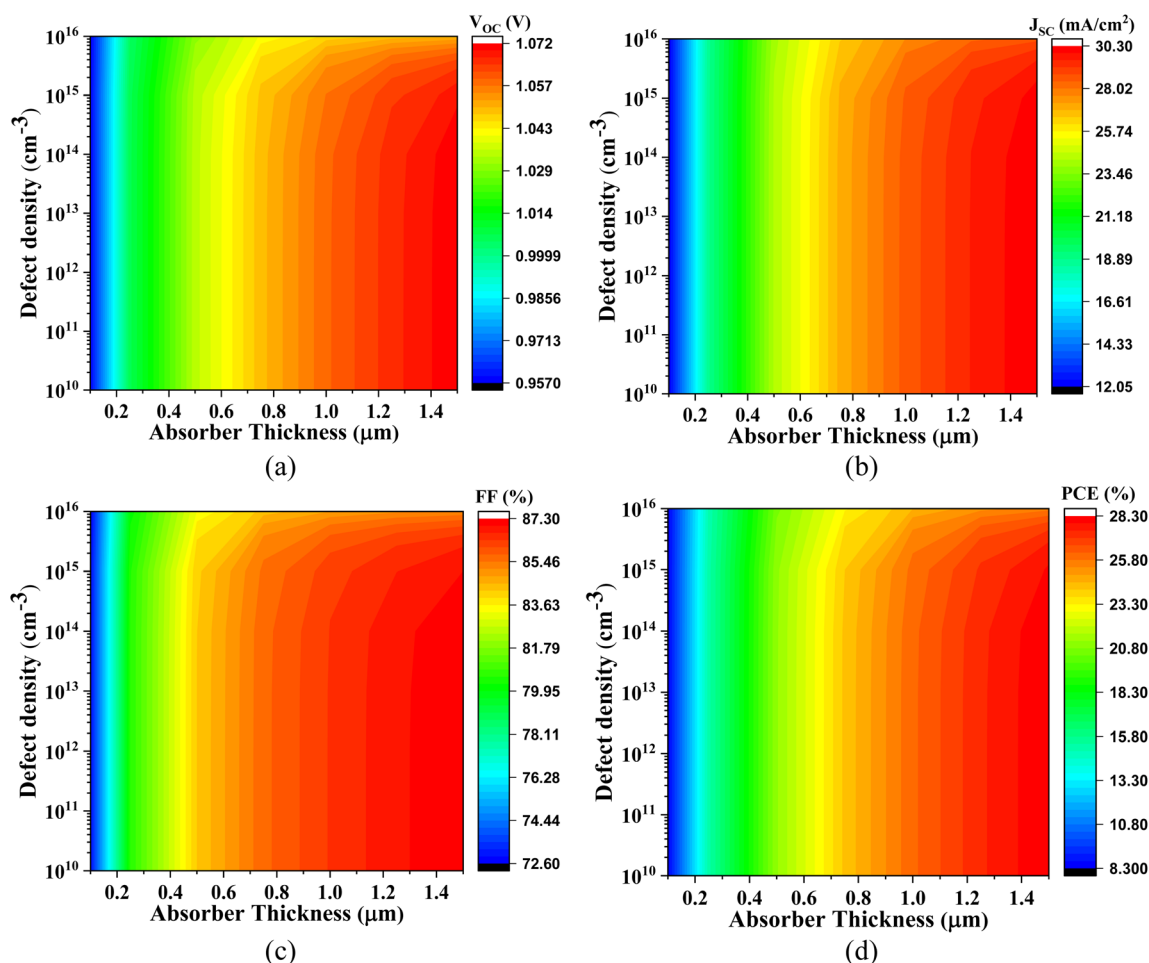


Fig. 12 Effect of active layer thickness and defect density on (a)  $V_{\text{OC}}$ , (b)  $J_{\text{SC}}$ , (c) FF, and (d) PCE of  $\text{Cs}_2\text{SnBr}_6$ -based PSC with  $\text{SnS}_2$  ETL.



Fig. 4(b) focuses on devices utilizing IGZO as the ETL. This configuration shows an increase in  $V_{OC}$  from 1.181 V to 1.233 V and  $J_{SC}$  from 9.53 mA cm<sup>-2</sup> to 20.07 mA cm<sup>-2</sup>. The FF follows a nearly linear growth, and the PCE improves from 8.88% to 23.61%. For Cs<sub>2</sub>SnBr<sub>6</sub>, the  $V_{OC}$  increases from 0.949 V to 1.070 V, while the  $J_{SC}$  rises sharply from 12.27 mA cm<sup>-2</sup> to 30.12 mA cm<sup>-2</sup>, attributed to the excellent carrier mobility and transparency of IGZO facilitating enhanced optical and electrical performance. The FF improves from 72.54% to 87.29%, and the PCE reaches up to 28.34%. Cs<sub>2</sub>SnI<sub>6</sub> exhibits almost constant trend across all four parameters, emphasizing the stable interfacial energetics and minimal recombination losses with IGZO as ETL.

Fig. 4(c) explores the performance with SnS<sub>2</sub> as the ETL. The  $V_{OC}$  for all absorbers shows an approximately linear increase with thickness, which reflects the gradual reduction in defect-assisted recombination at the interface. The  $J_{SC}$  increases from 10.37 mA cm<sup>-2</sup> to 23.18 mA cm<sup>-2</sup> for Cs<sub>2</sub>SnCl<sub>6</sub> and from 12.06 mA cm<sup>-2</sup> to 30.27 mA cm<sup>-2</sup> for Cs<sub>2</sub>SnBr<sub>6</sub>, primarily due to enhanced optical absorption. Notably, Cs<sub>2</sub>SnI<sub>6</sub> continues to exhibit a very high  $J_{SC}$  across all thickness values, further confirming its excellent photon harvesting capacity due to its narrow bandgap. The FF exhibits a linear trend for Cs<sub>2</sub>SnCl<sub>6</sub> and Cs<sub>2</sub>SnI<sub>6</sub>, while for Cs<sub>2</sub>SnBr<sub>6</sub>, it increases significantly from

72.86% to 87.27%, demonstrating excellent interface passivation and charge extraction with SnS<sub>2</sub>. Consequently, the PCE values rise appreciably: from 9.64% to 22.44% for Cs<sub>2</sub>SnCl<sub>6</sub>, from 8.42% to 28.29% for Cs<sub>2</sub>SnBr<sub>6</sub>, and from 21.14% to 24.95% for Cs<sub>2</sub>SnI<sub>6</sub>.

Fig. 4(d) evaluates the variation in absorber thickness for devices employing ZnS as the ETL. The  $V_{OC}$  follows a linear trend for all three absorbers, with Cs<sub>2</sub>SnBr<sub>6</sub> increasing from 0.931 V to 1.076 V, and Cs<sub>2</sub>SnCl<sub>6</sub> and Cs<sub>2</sub>SnI<sub>6</sub> remaining relatively constant around 1.08 V and 1.43 V, respectively. For Cs<sub>2</sub>SnCl<sub>6</sub>,  $J_{SC}$  increases from 9.74 mA cm<sup>-2</sup> to 23.17 mA cm<sup>-2</sup>, the FF rises from 62.40% to 72.15%, and the PCE improves from 10.74% to 25.58%. Similarly, for Cs<sub>2</sub>SnBr<sub>6</sub>,  $J_{SC}$  increases from 12.42 mA cm<sup>-2</sup> to 30.42 mA cm<sup>-2</sup>, but the FF slightly decreases from 77.09% to 76.02%, possibly due to charge accumulation or interfacial defects. Despite this, the PCE improves significantly from 7.39% to 23.62%.

In stark contrast, device with ZnS ETL suffer from a very low  $J_{SC}$  (~0.45 mA cm<sup>-2</sup>), attributed to unfavorable band alignment and strong charge blocking at the ZnS/absorber interface. The FF, however, follows a linear increase starting from 36.48%, and the PCE rises gradually from 0.175%, albeit remaining considerably lower than those of other configurations.

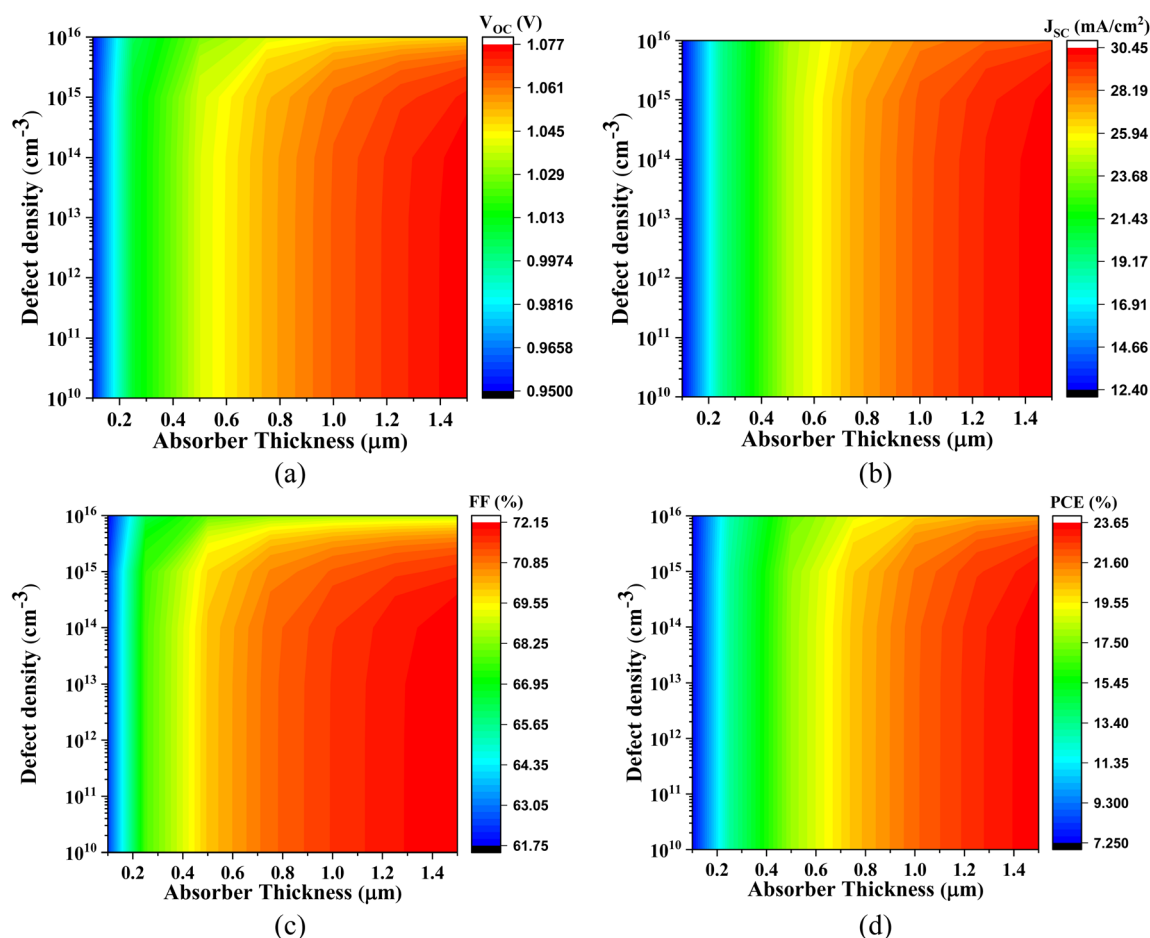


Fig. 13 Impact of absorber thickness and defect density on (a)  $V_{OC}$ , (b)  $J_{SC}$ , (c) FF, and (d) PCE of Cs<sub>2</sub>SnBr<sub>6</sub>-based PSC with ZnS ETL.



**3.2.2 Optimization of doping concentration of the absorber layer.** The effect of doping concentration in  $\text{Cs}_2\text{SnCl}_6$ ,  $\text{Cs}_2\text{SnBr}_6$ ,  $\text{Cs}_2\text{SnI}_6$  within a range of  $10^{12}$  to  $10^{19} \text{ cm}^{-3}$  with different ETLs is shown in Fig. 5.

In Fig. 5(a), the impact of varying the doping concentration of the absorber with CdS as the ETL is shown. For  $\text{Cs}_2\text{SnCl}_6$ , the  $V_{\text{OC}}$  is 1.215 V and follows a linear trend. The  $J_{\text{SC}}$  decreases from  $22.76 \text{ mA cm}^{-2}$  to  $19.86 \text{ mA cm}^{-2}$ , the FF increases from 82.52% to 86.12%, and the PCE decreases from 22.82% to 20.81%. For  $\text{Cs}_2\text{SnBr}_6$ , the  $V_{\text{OC}}$  increases from 0.862 V to 1.781 V, the  $J_{\text{SC}}$  decreases from  $33.03 \text{ mA cm}^{-2}$  to  $27.62 \text{ mA cm}^{-2}$ , the FF increases from 84.78% to 89.26%, and the PCE increases from 24.16% to 28.85%. For  $\text{Cs}_2\text{SnI}_6$ , the  $V_{\text{OC}}$ ,  $J_{\text{SC}}$ , FF, and PCE all show a linear trend. Fig. 5(b) shows the variation in absorber doping with IGZO as the ETL. For  $\text{Cs}_2\text{SnCl}_6$  with IGZO as the ETL, the  $V_{\text{OC}}$  is 1.231 V and follows a linear trend. The  $J_{\text{SC}}$  decreases linearly, from  $22.63 \text{ mA cm}^{-2}$ , the FF is 83.15% and also follows a linear trend, while the PCE is 23.19% and shows a linear variation. For  $\text{Cs}_2\text{SnBr}_6$ , the  $V_{\text{OC}}$  increases from 0.861 V to 1.178 V, the  $J_{\text{SC}}$  increases from  $32.91 \text{ mA cm}^{-2}$  to  $27.35 \text{ mA cm}^{-2}$ , the FF increases from 84.38% to 89.18%, and the PCE increases from 24.06% to 28.76%. For  $\text{Cs}_2\text{SnI}_6$ , the  $V_{\text{OC}}$  is 0.452 V and follows a linear trend.

The  $J_{\text{SC}}$  decreases from  $38.00 \text{ mA cm}^{-2}$  to  $33.45 \text{ mA cm}^{-2}$ , the FF is 57.21% and follows a constant trend, while the PCE decreases from 9.38% to 8.71%. Fig. 5(c) shows the variation in absorber doping with  $\text{SnS}_2$  as the ETL. For  $\text{Cs}_2\text{SnCl}_6$ , the  $V_{\text{OC}}$  is 1.175 V and follows a linear trend. The  $J_{\text{SC}}$  decreases from  $22.76 \text{ mA cm}^{-2}$  in a linear fashion, the FF increases from 82.12% to 85.75%, and the PCE decreases from 21.96% to 20.09%. For  $\text{Cs}_2\text{SnBr}_6$ , the  $V_{\text{OC}}$  increases from 0.861 V to 1.179 V, the FF rises from 84.76% to 89.46%, the  $J_{\text{SC}}$  decreases from  $35.03 \text{ mA cm}^{-2}$  to  $27.35 \text{ mA cm}^{-2}$ , and the PCE increases from 24.16% to 28.98%. For  $\text{Cs}_2\text{SnI}_6$ , the  $V_{\text{OC}}$ ,  $J_{\text{SC}}$ , FF, and PCE all follow linear trends.

Fig. 5(d) illustrates the variation in absorber doping with ZnS as the ETL. For  $\text{Cs}_2\text{SnCl}_6$ , the  $V_{\text{OC}}$  increases from 0.451 V to 1.481 V, while the  $J_{\text{SC}}$  decreases from  $22.76 \text{ mA cm}^{-2}$  to  $19.79 \text{ mA cm}^{-2}$ . The FF starts at 75.77% and follows a linear trend, and the PCE decreases from 25.00% to 22.42%. For  $\text{Cs}_2\text{SnBr}_6$ , the  $V_{\text{OC}}$  increases from 0.872 V to 1.212 V, the FF rises from 65.60% to 73.81%, the  $J_{\text{SC}}$  decreases from  $33.03 \text{ mA cm}^{-2}$  to  $23.78 \text{ mA cm}^{-2}$ , and the PCE decreases from 18.78% to 4.99%. For  $\text{Cs}_2\text{SnI}_6$ , the  $V_{\text{OC}}$ ,  $J_{\text{SC}}$ , FF, and PCE all show constant trends.

**3.2.3 Influence of thickness and defect density of  $\text{Cs}_2\text{SnZ}_6$  absorber.** This section discusses the influence of thickness and

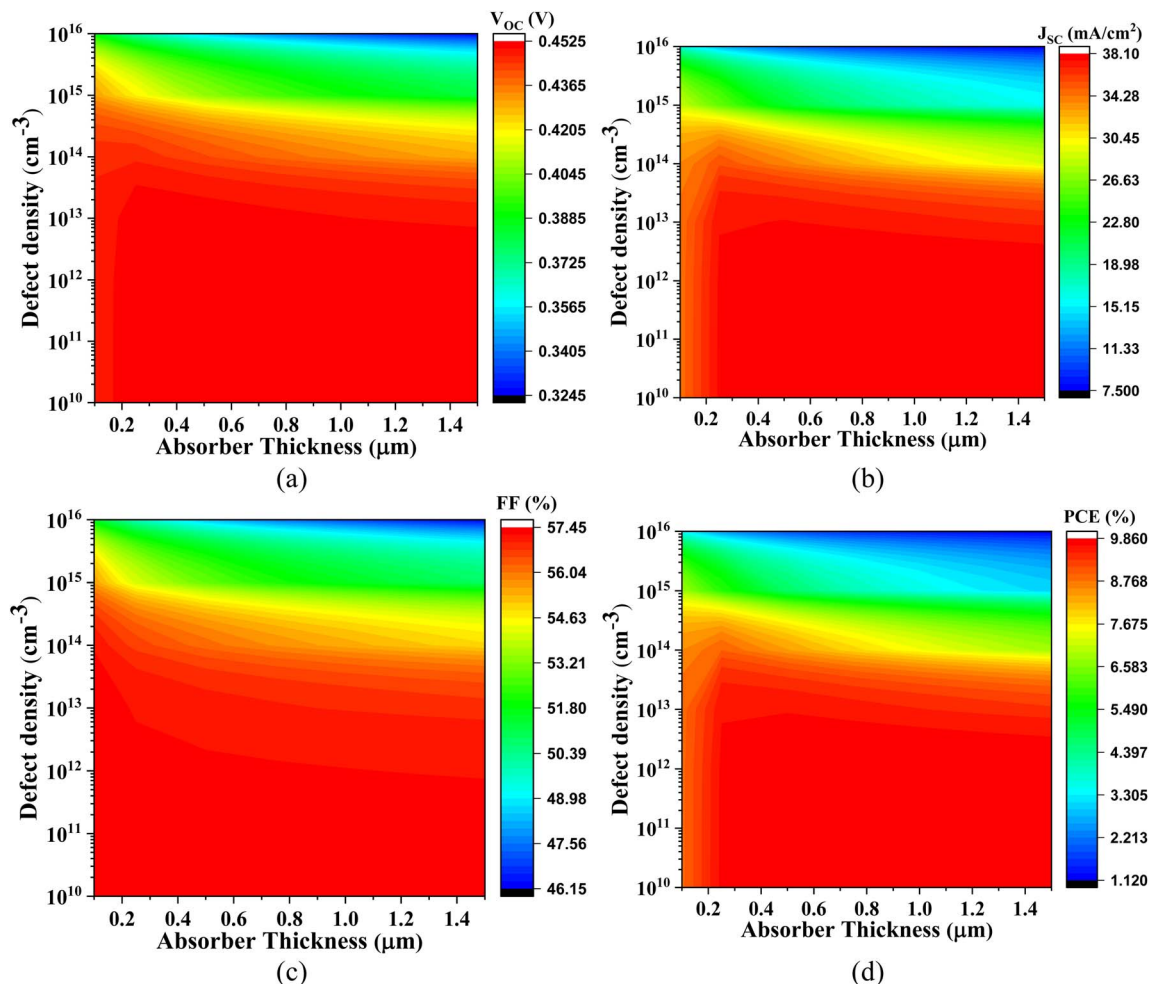


Fig. 14 Impact of active layer thickness and defect density on (a)  $V_{\text{OC}}$ , (b)  $J_{\text{SC}}$ , (c) FF, and (d) PCE of  $\text{Cs}_2\text{SnI}_6$ -based PSC with IGZO ETL.



defect density on the  $\text{Cs}_2\text{SnZ}_6$  absorbers. It examines how the thickness (ranging from 0.1 to 1.5  $\mu\text{m}$ ) and defect density (Nt) (ranging from  $10^{10}$  to  $10^{16} \text{ cm}^{-3}$ ) affect the PV output.

**3.2.3.1 Influence thickness and defect density of  $\text{Cs}_2\text{SnBr}_6$  absorber.** The graphical representations in Fig. 6 through 9 underscore that increasing the absorber layer thickness generally enhances photovoltaic performance metrics, particularly when defect density is maintained at a low level ( $\sim 10^{12} \text{ cm}^{-3}$ ). This enhancement can be attributed to two primary physical factors: improved photon absorption and more effective charge carrier generation. Thicker absorber layers increase the optical path length, allowing more incident photons to be absorbed and thus generating a higher number of electron-hole pairs. However, the benefits are contingent on the minimization of bulk and interface defects, which otherwise act as recombination centers, particularly detrimental in thicker films.

Fig. 6 displays the photovoltaic characteristics of  $\text{Cs}_2\text{SnCl}_6$  integrated with IGZO as the ETL. With absorber thicknesses exceeding 1.0  $\mu\text{m}$  and a low defect density of  $\sim 10^{12} \text{ cm}^{-3}$ , the  $V_{\text{OC}}$  ranges from 1.185 V to 1.206 V, the  $J_{\text{SC}}$  varies from 9.741 to 23.180  $\text{mA cm}^{-2}$ , the FF spans 69.39% to 77.09%, and the PCE increases from 10.23% to 25.28%. The notable improvement in  $J_{\text{SC}}$  and PCE is primarily due to enhanced light absorption and

reduced recombination, facilitated by the excellent band alignment and high electron mobility of IGZO, which supports efficient charge extraction.

Fig. 7 presents the performance of  $\text{Cs}_2\text{SnCl}_6$ -based PSC with CdS ETL. At absorber thicknesses ranging from 0.1  $\mu\text{m}$  to 1.0  $\mu\text{m}$ , the  $V_{\text{OC}}$  increases from 1.172 V to 1.216 V,  $J_{\text{SC}}$  ranges from 10.104  $\text{mA cm}^{-2}$  to 23.179  $\text{mA cm}^{-2}$ , FF improves from 76.74% to 82.73%, and PCE varies from 9.76% to 23.33%. These improvements are physically justified by the favorable conduction band offset between CdS and  $\text{Cs}_2\text{SnCl}_6$ , which minimizes electron-hole recombination at the interface. The observed trends also indicate that even moderately thin absorbers can perform well when the interface quality is high and defect densities are low.

Fig. 8 demonstrates the photovoltaic behavior of the  $\text{Cs}_2\text{SnCl}_6$ -based PSC with  $\text{SnS}_2$  ETL. For absorber thicknesses between 0.1  $\mu\text{m}$  and 1.0  $\mu\text{m}$  and under low-defect conditions,  $V_{\text{OC}}$  varies from 1.135 V to 1.176 V,  $J_{\text{SC}}$  spans from 10.375  $\text{mA cm}^{-2}$  to 23.179  $\text{mA cm}^{-2}$ , FF ranges from 76.74% to 82.32%, and PCE lies between 9.58% and 22.45%. Although  $\text{SnS}_2$  offers suitable band alignment, the relatively lower  $V_{\text{OC}}$  values compared to other configurations may be attributed to its

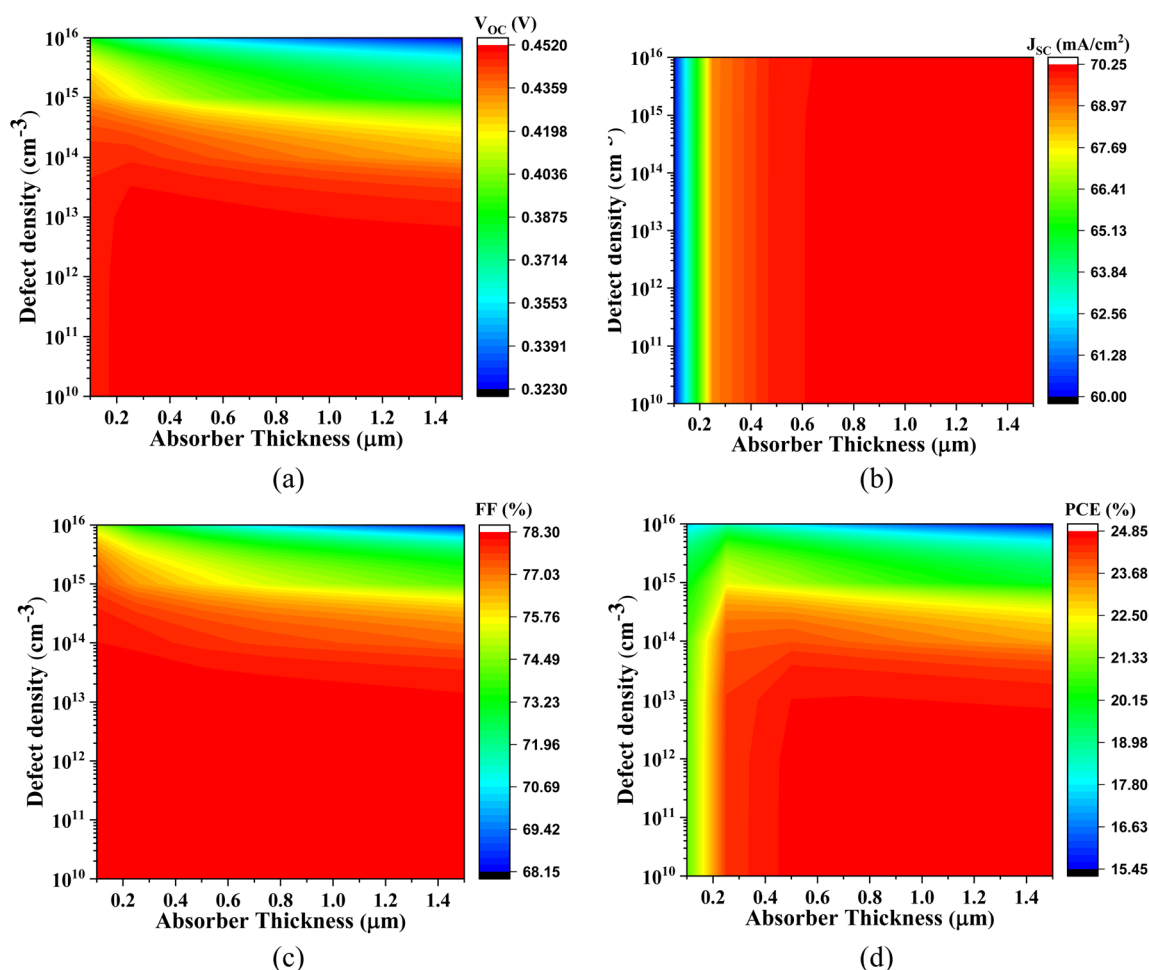


Fig. 15 Influence of absorber thickness and defect density on (a)  $V_{\text{OC}}$ , (b)  $J_{\text{SC}}$ , (c) FF, and (d) PCE of  $\text{Cs}_2\text{SnI}_6$ -based PSC with CdS ETL.



moderate electron mobility and higher interface defect density, which can result in non-radiative recombination losses.

Fig. 9 presents the most promising results with the  $\text{Cs}_2\text{SnCl}_6$ -based PSC with ZnS ETL. With an absorber thickness of 0.1–1.0  $\mu\text{m}$  and defect density around  $10^{12} \text{ cm}^{-3}$ , the  $V_{\text{OC}}$  ranges from 1.370 V to 1.451 V,  $J_{\text{SC}}$  increases from  $9.735 \text{ mA cm}^{-2}$  to  $23.180 \text{ mA cm}^{-2}$ , FF spans 69.39% to 76.09%, and PCE reaches up to 25.58%. The superior  $V_{\text{OC}}$  values observed in this configuration are likely due to the excellent CB alignment between ZnS and  $\text{Cs}_2\text{SnCl}_6$ , which creates a substantial built-in electric field that facilitates efficient charge separation and suppresses recombination.

**3.2.3.2 Effect thickness and defect density of  $\text{Cs}_2\text{SnBr}_6$  absorber.** Fig. 10 through 13 comprehensively illustrate the impact of defect density and absorber layer thickness on critical photovoltaic parameters for  $\text{Cs}_2\text{SnBr}_6$ -based solar cells employing various ETLs. Subfigures (a–d) within each figure delineate how these performance parameters evolve as a function of absorber thickness (ranging from 0.1 to 1.5  $\mu\text{m}$ ) and defect density, thereby enabling a detailed comparative assessment.

Fig. 10 presents the performance behavior of the  $\text{Cs}_2\text{SnBr}_6$ -based PSC with IGZO ETL. The  $V_{\text{OC}}$  varies from 0.946 V to

1.071 V, attributable to improved internal electric field strength and reduced interfacial recombination with increasing thickness and low defect densities. The  $J_{\text{SC}}$  spans from  $12.269 \text{ mA cm}^{-2}$  to  $30.269 \text{ mA cm}^{-2}$ , driven by enhanced photon absorption and more efficient photogenerated carrier transport in thicker absorber layers. The FF increases from 71.88% to 87.29%, primarily due to the suppression of trap-assisted recombination and improved carrier extraction dynamics. Consequently, the PCE improves significantly from 8.34% to 28.34%. However, higher defect densities introduce non-radiative recombination centers, leading to degraded charge collection efficiency and diminished values across all photovoltaic parameters.

Fig. 11 highlights the performance of the  $\text{Cs}_2\text{SnBr}_6$ -based PSC with CdS ETL. The  $V_{\text{OC}}$  increases from 0.956 V to 1.072 V, facilitated by favorable CB alignment and a strong built-in potential that minimizes carrier recombination. The  $J_{\text{SC}}$  increases from  $11.75 \text{ mA cm}^{-2}$  to  $30.25 \text{ mA cm}^{-2}$  with absorber thickening, due to greater light absorption and longer carrier diffusion lengths. The FF improves from 71.90% to 87.25%, reflecting reduced series resistance and enhanced interfacial charge transport. Accordingly, the PCE increases from 8.00% to 28.34%. As with other structures, the rise in defect density

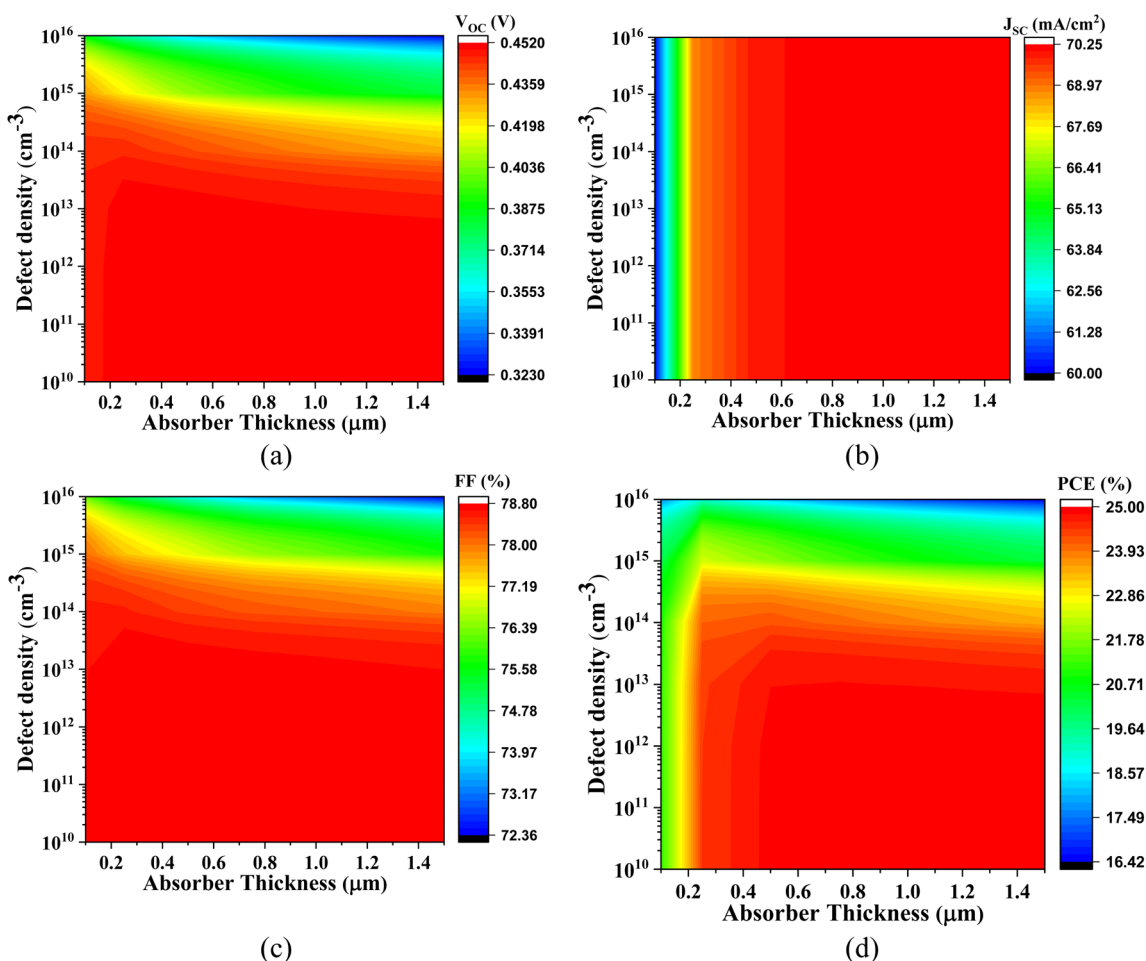


Fig. 16 Impact of absorber layer thickness and defect density on (a)  $V_{\text{OC}}$ , (b)  $J_{\text{SC}}$ , (c) FF, and (d) PCE of  $\text{Cs}_2\text{SnI}_6$ -based PSC with  $\text{SnS}_2$  ETL.



deteriorates all key parameters due to an escalation in bulk recombination and a decline in quasi-Fermi level splitting.

Fig. 12 demonstrates the performance metrics for the  $\text{Cs}_2\text{SnBr}_6$ -based PSC with  $\text{SnS}_2$  ETL. Here, the  $V_{\text{OC}}$  ranges from 0.957 V to 1.070 V, influenced by interfacial recombination dynamics and electrostatic potential alignment. The  $J_{\text{SC}}$  improves from  $12.05 \text{ mA cm}^{-2}$  to  $30.30 \text{ mA cm}^{-2}$ , stemming from effective photogeneration and reduced carrier trapping in thicker absorbers. The FF rises from 72.55% to 87.30%, reflecting efficient charge collection at the ETL interface. These favorable characteristics translate into a notable increase in PCE from 8.30% to 28.30%. Nevertheless, performance degrades at higher defect densities, as recombination pathways become more pronounced, especially at mid-gap states.

Fig. 13 depicts the photovoltaic behavior of  $\text{Cs}_2\text{SnBr}_6$ -based PSC with ZnS ETL. The  $V_{\text{OC}}$  increases from 0.95 V to 1.08 V with increasing absorber thickness, attributed to reduced recombination losses and improved electrostatic potential profiles. The  $J_{\text{SC}}$  ranges from  $12.43 \text{ mA cm}^{-2}$  to  $30.42 \text{ mA cm}^{-2}$ , due to enhanced optical absorption and improved carrier lifetime. However, the FF, which varies from 61.75% to 72.12%, is comparatively lower than in other configurations—likely due to unfavorable energy band alignment and increased resistive

losses at the  $\text{Cs}_2\text{SnBr}_6/\text{ZnS}$  interface. As a result, the PCE ranges from 7.29% to 23.62%. Once again, increased defect densities lead to a consistent decline across all metrics, reaffirming the critical role of material quality in achieving high-performance lead-free perovskite photovoltaics.

**3.2.3.3 Influence thickness and defect density of  $\text{Cs}_2\text{SnI}_6$  absorber.** Owing to the intrinsically narrow bandgap of the  $\text{Cs}_2\text{SnI}_6$  absorber, the PV performance characteristics of this material interfaced with various ETLs are systematically presented in Fig. 14–17, respectively.

Fig. 14 illustrates the device behavior of the  $\text{Cs}_2\text{SnI}_6$ -based PSC with IGZO ETL. The  $V_{\text{OC}}$  ranges from 0.32 V to 0.45 V, constrained primarily by the low quasi-Fermi level splitting associated with the narrow bandgap of  $\text{Cs}_2\text{SnI}_6$ . In contrast, the short-circuit current density  $J_{\text{SC}}$  spans a remarkably high range, from  $60.04 \text{ mA cm}^{-2}$  to  $70.20 \text{ mA cm}^{-2}$ , driven by the strong photon absorption capacity in the visible to near-infrared spectral regions. The FF ranges from 76.17% to 78.78%, reflecting moderate carrier transport efficiency and minimal recombination losses. As a result, the PCE improves from 16.42% to 25.98%, highlighting the absorber's superior light-harvesting ability despite its limited photovoltage.

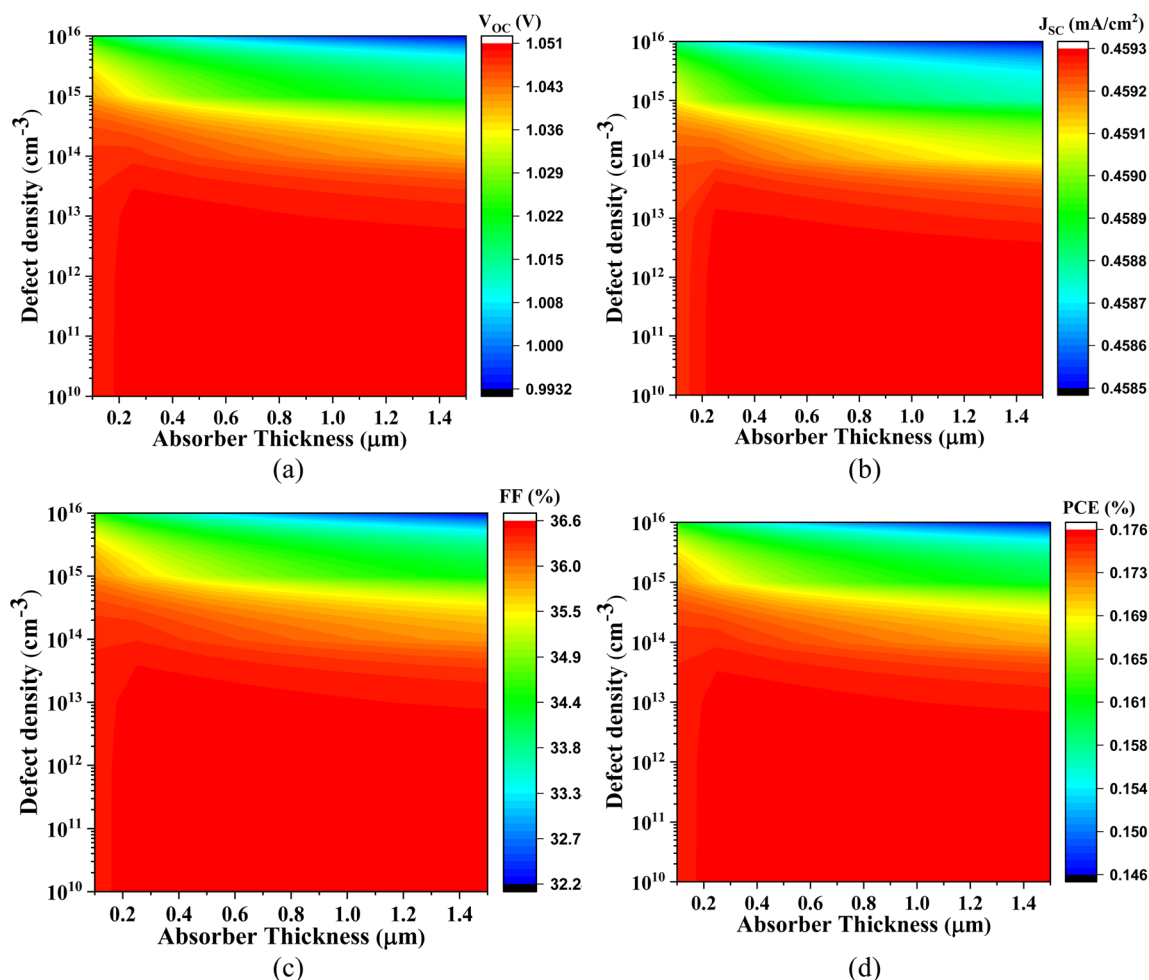


Fig. 17 Effect of active layer thickness and defect density on (a)  $V_{\text{OC}}$ , (b)  $J_{\text{SC}}$ , (c) FF, and (d) PCE of  $\text{Cs}_2\text{SnI}_6$ -based PSC with ZnS ETL.



Table 3 Obtained PV output with optimized parameters

ETL	Parameters			
	$V_{OC}$ (V)	$J_{SC}$ ( $\text{mA cm}^{-2}$ )	FF (%)	PCE (%)
<b>Cs<sub>2</sub>SnCl<sub>6</sub>-based PSC</b>				
IGZO	1.232	22.60	83.00	23.11
SnS <sub>2</sub>	1.175	22.71	82.30	21.97
CdS	1.215	22.71	82.72	22.83
ZnS	1.450	22.71	76.05	25.05
<b>Cs<sub>2</sub>SnBr<sub>6</sub>-based PSC</b>				
IGZO	1.059	28.65	86.44	26.22
SnS <sub>2</sub>	1.059	25.54	86.41	26.12
CdS	1.059	28.50	86.37	26.07
ZnS	1.063	28.74	71.52	21.87
<b>Cs<sub>2</sub>SnI<sub>6</sub>-based PSC</b>				
IGZO	0.452	37.99	57.22	9.82
SnS <sub>2</sub>	0.451	70.17	78.78	24.95
CdS	0.451	70.18	78.28	24.80
ZnS	1.050	0.46	36.60	0.18

Table 3 presents the optimized PV performance parameters for Cs<sub>2</sub>SnCl<sub>6</sub>, Cs<sub>2</sub>SnBr<sub>6</sub>, and Cs<sub>2</sub>SnI<sub>6</sub>-based devices employing different ETLs. For Cs<sub>2</sub>SnCl<sub>6</sub>-based PSC, ZnS yields the highest PCE of 25.05%, attributed to its relatively high  $V_{OC}$  = 1.450 V, despite a modest FF (76.05%). Cs<sub>2</sub>SnBr<sub>6</sub>-based devices achieve comparable maximum efficiencies, with IGZO delivering the highest PCE of 26.22%, driven by its superior  $J_{SC}$  (28.65  $\text{mA cm}^{-2}$ ) and FF (86.44%), although the  $V_{OC}$  remains modest. In contrast, Cs<sub>2</sub>SnI<sub>6</sub> exhibits the most significant variation among ETLs: while SnS<sub>2</sub> and CdS facilitate excellent performance (PCEs  $\approx$  25%) due to very high  $J_{SC}$  values ( $>70 \text{ mA cm}^{-2}$ ), the ZnS-based device performs poorly (PCE = 0.18%) owing to a drastic reduction in  $J_{SC}$  and FF, indicating strong charge blocking and poor band alignment.

Fig. 15 depicts the PV behavior of Cs<sub>2</sub>SnI<sub>6</sub>-based PSC with CdS ETL, where the  $V_{OC}$  similarly varies between 0.32 V and

0.45 V, again limited by the narrow absorber bandgap. The  $J_{SC}$  increases from 60.00  $\text{mA cm}^{-2}$  to 70.25  $\text{mA cm}^{-2}$ , benefiting from the extended spectral absorption. However, the FF ranges from 68.15% to 78.30%, slightly lower than that of IGZO, possibly due to increased interface recombination or less favorable band alignment at the CdS/Cs<sub>2</sub>SnI<sub>6</sub> interface. Accordingly, the PCE ranges from 15.45% to 24.85%.

Fig. 16 presents the photovoltaic response of Cs<sub>2</sub>SnI<sub>6</sub>-based PSC with SnS<sub>2</sub> ETL. The  $V_{OC}$  values range from 0.323 V to 0.452 V, following similar trends dictated by the fundamental bandgap limitations. The  $J_{SC}$  values remain robust, ranging from 60.00  $\text{mA cm}^{-2}$  to 70.20  $\text{mA cm}^{-2}$ , due to effective light absorption and favorable optical constants. The FF spans from 72.40% to 78.80%, indicating improved charge extraction and reduced series resistance relative to CdS. These features collectively yield a PCE between 16.40% and 25.00%, signifying a promising device configuration.

Fig. 17, in contrast, delineates the device metrics for the Cs<sub>2</sub>SnI<sub>6</sub>-based PSC with ZnS ETL. In this configuration, the  $V_{OC}$  shows unusually high values, ranging from 0.99 V to 1.05 V, which may arise due to an unfavorable energy band offset at the ZnS/Cs<sub>2</sub>SnI<sub>6</sub> interface that hinders effective carrier recombination and artificially elevates the  $V_{OC}$ . However, this comes at a significant trade-off: the  $J_{SC}$  is extremely low, varying only between 0.45  $\text{mA cm}^{-2}$  and 0.46  $\text{mA cm}^{-2}$ , which is attributed to excessive interfacial carrier blocking and poor electron injection efficiency, owing to the large bandgap and poor energy level alignment of ZnS. The FF ranges from only 32.24% to 36.61%, likely due to high series resistance and severe charge accumulation at the interface. Consequently, the PCE drops sharply to a mere 0.16–0.18%, indicating the unsuitability of ZnS as an ETL for Cs<sub>2</sub>SnI<sub>6</sub>-based solar cells.

### 3.3 $J$ - $V$ and QE characteristics corresponding to variations in absorber layer thickness of the optimized device

The  $J$ - $V$  and QE characteristics presented in Fig. 18(a) and (b), respectively, illustrate the influence of varying the Cs<sub>2</sub>SnBr<sub>6</sub>

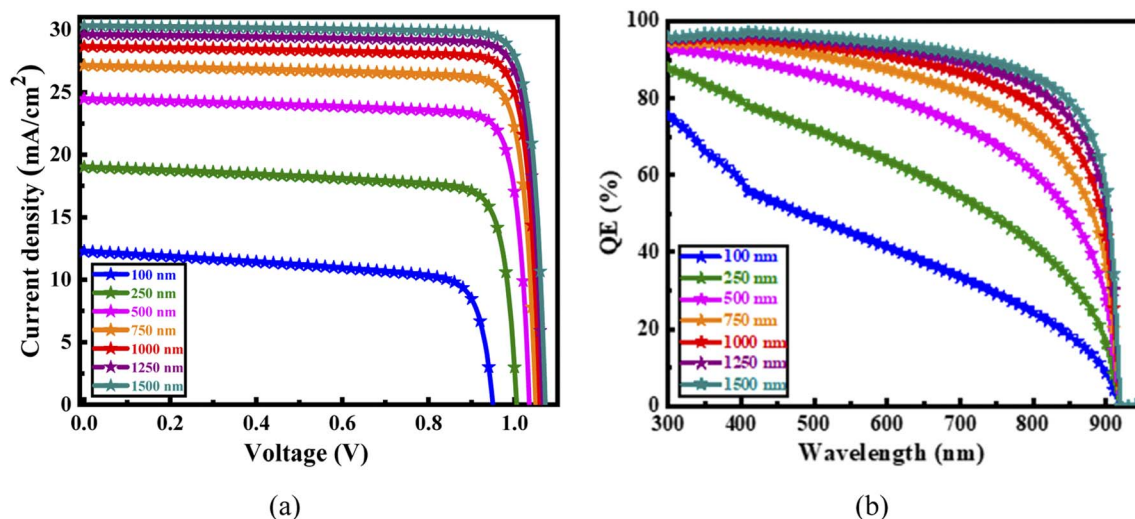


Fig. 18 (a) Current–voltage and (b) quantum efficiency characteristics of the optimized device as a function of absorber layer thickness.



Table 4 Comparative performance metrics of Cs<sub>2</sub>SnX<sub>6</sub>-based solar cell configurations<sup>a</sup>

Type	Structure	V <sub>OC</sub> (V)	J <sub>SC</sub> (mA cm <sup>-2</sup> )	FF (%)	PCE (%)	Ref.
E	FTO/TiO <sub>2</sub> /Cs <sub>2</sub> SnI <sub>6</sub> /P3HT	0.52	3.2	51.5	0.86	70
E	FTO/TiO <sub>2</sub> /Cs <sub>2</sub> SnI <sub>6</sub> /Dye	0.67	16.3	61.8	6.8	71
E	FTO/TiO <sub>2</sub> /Cs <sub>2</sub> SnI <sub>6</sub>	0.67	12.56	0.50	4.23	72
S	ITO/CuI/Cs <sub>2</sub> SnI <sub>6</sub> /PCBM	0.86	23.91	71.08	14.65	73
S	FTO/TiO <sub>2</sub> /Cs <sub>2</sub> SnI <sub>6</sub> /Cu <sub>2</sub> O	0.74	30.00	80.50	17.77	74
S	FTO/SnS <sub>2</sub> /Cs <sub>2</sub> SnI <sub>6</sub>	0.451	70.17	78.78	24.95	This work(optimized)
S	FTO/ZnS/Cs <sub>2</sub> SnCl <sub>6</sub>	1.45	22.71	76.05	25.05	This work(optimized)
S	FTO/IGZO/Cs <sub>2</sub> SnBr <sub>6</sub>	1.059	28.65	86.44	26.22	This work(optimized)

<sup>a</sup> E = experimental, S = simulation.

absorber layer thickness on the photovoltaic performance of solar cells employing an IGZO ETL. As shown in Fig. 18(a), both the  $J_{SC}$  and  $V_{OC}$  increase progressively with absorber thickness from 100 nm to 1500 nm, primarily due to enhanced light absorption and reduced interface recombination. The device with a 1500 nm thick absorber achieves the highest  $J_{SC}$  and  $V_{OC}$ , reflecting superior carrier generation and collection.<sup>69</sup> However, the performance improvement beyond 1000 nm is marginal, while the potential for increased recombination and material usage becomes more significant. Therefore, 1000 nm is considered the optimal thickness, offering a favorable balance between high efficiency and material economy. The trend is further corroborated by the QE spectra in Fig. 18(b), where QE improves with thickness due to stronger photon absorption, with the 1000 nm to 1500 nm devices exhibiting the most effective spectral response across the visible and near-infrared regions. In contrast, thinner devices, particularly at 100 nm and 250 nm, exhibit noticeably lower QE and  $J_{SC}$  values due to insufficient absorption depth and weaker charge carrier collection.

Table 4 provides a comprehensive comparative analysis of Cs<sub>2</sub>SnX<sub>6</sub>-based perovskite solar cells, highlighting key findings from both experimental investigations and simulation-based studies to evaluate their performance and potential for photovoltaic applications.

## 4. Conclusions

In this work, we conducted an in-depth first-principles and numerical evaluation of Cs<sub>2</sub>SnZ<sub>6</sub> compounds as lead-free photovoltaic absorbers. DFT-based analyses confirmed their structural integrity, direct bandgaps, and strong optical absorption, with clear trends linking halide substitution to bandgap narrowing and enhanced light-harvesting capacity. SCAPS-1D simulations further elucidated the influence of absorber thickness, doping concentration, and defect density on device performance, revealing that absorber layers exceeding 1000 nm and low bulk defect densities significantly enhance photovoltaic efficiency. Among the investigated configurations, the Al/FTO/IGZO/Cs<sub>2</sub>SnBr<sub>6</sub>/Au combination yielded the best performance (PCE = 26.22%), balancing favorable band alignment, carrier mobility, and optical properties. Conversely, Cs<sub>2</sub>SnI<sub>6</sub>, while offering high  $J_{SC}$  due to its narrow bandgap, was

limited by poor ETL compatibility in certain structures (*e.g.*, ZnS). Overall, this study underscores the viability of Cs<sub>2</sub>SnZ<sub>6</sub> perovskites in eco-friendly solar technologies and provides strategic guidance for material and device-level optimization to propel the development of high-performance, lead-free perovskite solar cells.

## Data availability

Data will be available on request.

## Conflicts of interest

There are no conflicts of interest to declare.

## Acknowledgements

The authors extend their appreciation to the Deanship of Research and Graduate Studies at King Khalid University for funding this work through Large Research Project under grant number RGP2/250/46.

## References

- M. K. Hossain, M. S. Uddin, G. F. I. Toki, M. K. A. Mohammed, R. Pandey, J. Madan, F. Rahman, R. Islam, S. Bhattarai, H. Bencherif, D. P. Samajdar, M. Amami and D. K. Dwivedi, *RSC Adv.*, 2023, **13**, 23514–23537.
- A. Kuddus, M. K. A. Mohammed, A. K. Al-mousoi, A. Ghosh, S. Bhattarai, R. Pandey, J. Madan and M. K. Hossain, *RSC Adv.*, 2023, 31330–31345.
- T. W. Kelley, P. F. Baude, C. Gerlach, D. E. Ender, D. Muires, M. A. Haase, D. E. Vogel and S. D. Theiss, *Chem. Mater.*, 2004, **16**, 4413–4422.
- I. S. Hajime Shirai, T. Ariyoshi and J.-i. Hanna, *J. Non-Cryst. Solids*, 1991, **137–138**, 693–696.
- M. Harun-Or-Rashid, L. Ben Farhat, A. Brahmia, M. K. A. Mohammed, M. A. Rahman, A. Azzouz-Rached and M. F. Rahman, *J. Mater. Sci.*, 2024, **59**, 6365–6385.
- M. S. Reza, M. F. Rahman, A. Kuddus, M. K. A. Mohammed, A. K. Al-Mousoi, M. R. Islam, A. Ghosh, S. Bhattarai,



- R. Pandey, J. Madan and M. K. Hossain, *RSC Adv.*, 2023, **13**, 31330–31345.
- 7 M. K. A. Mohammed, S. M. Abdalhadi, A. Kumar, O. P. Doshi, A. K. Al-mousoi, H. T. Hussein, R. S. Alnayli, J. Madan, A. M. Tawfeek, F. Rahman and M. K. Hossain, *Energy Fuels*, 2023, **37**, 19870–19881.
- 8 S. Bhattarai, M. K. Hossain, R. Pandey, J. Madan, D. P. Samajdar, M. F. Rahman, M. Z. Ansari and M. Amami, *Energy Fuels*, 2023, **37**, 10631–10641.
- 9 M. S. Reza, M. F. Rahman, A. Kuddus, M. S. Reza, M. A. Monnaf, M. R. Islam, S. Bhattarai, S. Al-Qaisi, L. Ben Farhat and S. Ezzine, *Energy Fuels*, 2024, **38**, 2327–2342.
- 10 M. K. Hossain, M. K. A. Mohammed, R. Pandey, A. A. Arnab, M. H. K. Rubel, K. M. Hossain, M. H. Ali, M. F. Rahman, H. Bencherif, J. Madan, M. R. Islam, D. P. Samajdar and S. Bhattarai, *Energy Fuels*, 2023, **37**, 6078–6098.
- 11 A. Ghosh, M. Ferdous Rahman, A. Kuddus, M. K. A. Mohammed, M. Rasidul Islam, S. Bhattarai, A. R. Chaudhry and A. Irfan, *J. Alloys Compd.*, 2024, 174097.
- 12 M. K. Hossain, A. A. Arnab, D. P. Samajdar, M. H. K. Rubel, M. M. Hossain, M. R. Islam, R. C. Das, H. Bencherif, M. F. Rahman, J. Madan, R. Pandey, S. Bhattarai, M. Amami and D. K. Dwivedi, *Energy Fuels*, 2023, **37**, 13377–13396.
- 13 A. Richter, R. Müller, J. Benick, F. Feldmann, B. Steinhauser, C. Reichel, A. Fell, M. Bivour, M. Hermle and S. W. Glunz, *Nat. Energy*, 2021, **6**, 429–438.
- 14 F. Hao, C. C. Stoumpos, D. H. Cao, R. P. H. Chang and M. G. Kanatzidis, *Nat. Photonics*, 2014, **8**, 489–494.
- 15 M. Wang, W. Wang, B. Ma, W. Shen, L. Liu, K. Cao, S. Chen and W. Huang, *Lead-free Perovskite Materials for Solar Cells*, Springer, Singapore, 2021, vol. 13.
- 16 M. K. Hossain, G. F. I. Toki, I. Alam, R. Pandey, D. P. Samajdar, M. F. Rahman, M. R. Islam, M. H. K. Rubel, H. Bencherif, J. Madan and M. K. A. Mohammed, *New J. Chem.*, 2023, **47**, 4801–4817.
- 17 M. F. Rahman, M. A. Rahman, M. R. Islam, A. Ghosh, M. A. Bashar Shanto, M. Chowdhury, M. Al Ijazul Islam, M. H. Rahman, M. K. Hossain and M. A. Islam, *AIP Adv.*, 2023, **13**, 2.
- 18 M. K. Hossain, G. F. Ishraque Toki, D. P. Samajdar, M. H. K. Rubel, M. Mushtaq, M. R. Islam, M. F. Rahman, S. Bhattarai, H. Bencherif, M. K. A. Mohammed, R. Pandey and J. Madan, *Energy Fuels*, 2023, **37**, 7380–7400.
- 19 M. Faizan, K. C. Bhamu, G. Murtaza, X. He, N. Kulhari, M. M. AL-Anazy and S. H. Khan, *Sci. Rep.*, 2021, **11**, 1–9.
- 20 A. Phys and W. Zhu, *Appl. Phys. Lett.*, 2019, **115**, 121106.
- 21 J. Zhou, J. Luo, X. Rong, P. Wei, M. S. Molokeev, Y. Huang, J. Zhao, Q. Liu, X. Zhang, J. Tang and Z. Xia, *Adv. Opt. Mater.*, 2019, **7**, 1–7.
- 22 G. Yuan, S. Huang, J. Niu, S. Qin, X. Wu, H. Ding and A. Lu, *Solid State Commun.*, 2018, **275**, 68–72.
- 23 M. G. Brik and I. V. Kityk, *J. Phys. Chem. Solids*, 2011, **72**, 1256–1260.
- 24 Z. Tan, J. Li, C. Zhang, Z. Li, Q. Hu, Z. Xiao, T. Kamiya, H. Hosono, G. Niu, E. Lifshitz, Y. Cheng and J. Tang, *Adv. Funct. Mater.*, 2018, **28**, 1–10.
- 25 X. Qing, C. Wu and X. Han, *Molecules*, 2023, **28**, 1–9.
- 26 M. Y. Arafat, S. F. Wan Muhammad Hatta, M. A. Islam, M. R. Johan and Y. Abdul Wahab, *ChemNanoMat*, 2025, **11**, e202500032.
- 27 A. V. Savita Rawat and J. Madan, in *2024 International Conference on Communication, Computing and Energy Efficient Technologies (I3CEET)*, IEEE, Gautam Buddha Nagar, India, 2024, pp. 681–684.
- 28 M. S. Uddin, M. K. Hossain, M. B. Uddin, G. F. I. Toki, M. Ouladsmene, M. H. K. Rubel, D. I. Tishkevich, P. Sasikumar, R. Haldhar and R. Pandey, *Adv. Electron. Mater.*, 2024, **10**, 2300751.
- 29 Naureen, Sadanand, P. Lohia, D. K. Dwivedi and S. Ameen, in *Solar*, MDPI, 2022, vol. 2, pp. 341–353.
- 30 A. Isha, A. Kowsar, A. Kuddus, M. K. Hossain, M. H. Ali, M. D. Haque and M. F. Rahman, *Heliyon*, 2023, **9**, e15716.
- 31 N. A. Jahan, S. I. Parash, M. A. Hossain and T. Chowdhury, *Chalcogenide Lett.*, 2024, **21**, 675–686.
- 32 A. Ayyaz, M. Kaleem, A. Nasir, N. D. Alkhalidi, M. mana Al-Anazy, I. Boukhris, Q. Mahmood and M. Z. Abbasi, *Sol. Energy*, 2025, **299**, 113738.
- 33 J. P. Perdew and A. Zunger, *Phys. Rev. B: Condens. Matter Mater. Phys.*, 1981, **23**, 5048–5079.
- 34 G. Kresse and J. Hafner, *J. Phys.: Condens. Matter*, 1994, **6**, 8245–8257.
- 35 J. P. Perdew, K. Burke and M. Ernzerhof, *Phys. Rev. Lett.*, 1996, **77**, 3865–3868.
- 36 M. F. Rahman, M. N. H. Toki, M. R. Islam, P. Barman, S. Chowdhury, M. Rasheduzzaman and M. Z. Hasan, *Opt. Quantum Electron.*, 2024, **56**, 206.
- 37 F. Rahman, M. Islam, R. Islam, A. Ghosh and Q. Mahmood, *J. Solid State Chem.*, 2023, **328**, 124341.
- 38 L. Krache, M. A. Ghebouli, B. Ghebouli, M. Fatmi, T. Chihi and S. I. Ahmed, *Acta Phys. Pol. A*, 2023, **143**, 3.
- 39 U. G. Jong, C. J. Yu and Y. H. Kye, *RSC Adv.*, 2019, **10**, 201–209.
- 40 M. Burgelman, P. Nollet and S. Degraeve, *Thin Solid Films*, 2000, **361–362**, 527–532.
- 41 M. H. Ali, M. A. Al Mamun, M. D. Haque, M. F. Rahman, M. K. Hossain and A. Z. Abu, *ACS Omega*, 2023, **8**, 7017–7029.
- 42 G. M. Dalpian, Q. Liu, C. C. Stoumpos, A. P. Douvalis, M. Balasubramanian, M. G. Kanatzidis and A. Zunger, *Phys. Rev. Mater.*, 2017, **1**, 1–10.
- 43 Y. Cai, W. Xie, H. Ding, Y. Chen, T. Krishnamoorthy, L. H. Wong, N. Mathews, S. G. Mhaisalkar, M. P. Sherburne and M. Asta, *Chem. Mater.*, 2017, **29**, 7740–7749.
- 44 G. Volonakis, A. A. Haghighirad, R. L. Milot, W. H. Sio, M. R. Filip, B. Wenger, M. B. Johnston, L. M. Herz, H. J. Snaith and F. Giustino, *J. Phys. Chem. Lett.*, 2017, **8**, 772–778.
- 45 S. Nair, M. Deshpande, V. Shah, S. Ghaisas and S. Jadkar, *J. Phys.: Condens. Matter*, 2019, **31**, 445902.
- 46 N. A. Noor, M. W. Iqbal, T. Zelai, A. Mahmood, H. M. Shaikh, S. M. Ramay and W. Al-Masry, *J. Mater. Res. Technol.*, 2021, **13**, 2491–2500.



- 47 A. Ayyaz, S. Saidi, N. Dawas Alkhaldi, G. Murtaza, N. Sfina and Q. Mahmood, *Sol. Energy*, 2024, **279**, 112844.
- 48 S. Saha, T. P. Sinha and A. Mookerjee, *Phys. Rev. B: Condens. Matter Mater. Phys.*, 2000, **62**, 8828–8834.
- 49 M. Q. Cai, Z. Yin and M. S. Zhang, *Appl. Phys. Lett.*, 2003, **83**, 2805–2807.
- 50 Y. Li, W. Fan, H. Sun, X. Cheng, P. Li and X. Zhao, *J. Phys.: Condens. Matter*, 2011, **23**, 225401.
- 51 A. B. Kuzmenko, *Rev. Sci. Instrum.*, 2005, **76**, 083108.
- 52 M. R. Islam, A. A. M. Mazumder, M. R. H. Mojumder, A. S. M. Z. Shifat and M. K. Hossain, *Jpn. J. Appl. Phys.*, 2023, **62**, 11002.
- 53 Z. Xie, L. Hui, J. Wang, G. Zhu, Z. Chen and C. Li, *Comput. Mater. Sci.*, 2018, **144**, 304–314.
- 54 R. Islam, K. Liu, Z. Wang, S. Hasan, Y. Wu, S. Qu and Z. Wang, *Mater. Today Commun.*, 2022, **31**, 103305.
- 55 Z. Xu, *Solid State Commun.*, 1990, **76**, 1143–1147.
- 56 M. R. Islam, A. S. M. J. Islam, K. Liu, Z. Wang, S. Qu, C. Zhao, X. Wang and Z. Wang, *Phys. B*, 2022, **638**, 413960.
- 57 M. A. Fadla, B. Bentría, T. Dahame and A. Benghia, *Phys. B*, 2020, **585**, 412118.
- 58 M. R. Islam, M. R. H. Mojumder, R. Moshwan, A. S. M. J. Islam, M. A. Islam, M. S. Rahman and M. H. Kabir, *ECS J. Solid State Sci. Technol.*, 2022, **11**, 33001.
- 59 A. Ayyaz, G. Murtaza, M. Shafiq, M. Qasim Shah, N. Sfina and S. Ali, *Sol. Energy*, 2023, **265**, 112131.
- 60 D. J. Chadi and R. M. White, *Phys. Rev. B*, 1975, **11**, 5077–5081.
- 61 G. M. Mustafa, B. Younas, A. Ayyaz, A. I. Aljameel, S. Alotaibi, S. Bouzgarrou, S. K. Ali, Q. Mahmood, I. Boukhris and M. S. Al-Buriahi, *RSC Adv.*, 2025, **15**, 5202–5213.
- 62 M. N. Islam, M. A. Hadi and J. Podder, *AIP Adv.*, 2019, **9**, 1–9.
- 63 A. Ayyaz, M. Zaman, H. D. Alkhaldi, H. I. Ali, I. Boukhris, S. Bouzgarrou, M. mana Al-Anazy and Q. Mahmood, *RSC Adv.*, 2025, **15**, 11128–11145.
- 64 M. Rahman, A. Lubaba, A. Irfan and M. F. Rahman, *ChemistrySelect*, 2024, **9**, e202403217.
- 65 Z. Rao, B. Du, C. Huang, L. Shu, P. Lin, N. Fu and S. Ke, *J. Alloys Compd.*, 2019, **789**, 276–281.
- 66 F. Rahman, M. Rahman, F. Hossain, B. Islam, S. Rashel, A. Ahmed and A. Irfan, *Adv. Photonics Res.*, 2024, 2400148.
- 67 M. Masum Mia, M. Faruk Hossain, M. Rahman, N. Badi, A. Irfan and M. Ferdous Rahman, *Mater. Sci. Eng., B*, 2025, **311**, 117817.
- 68 H. C. Bennett, T. R. A. Ashok, F. Joselin, N. R. E. Antony and R. J. Beula, *Opt. Mater.*, 2024, **154**, 115695.
- 69 E. Danladi, D. S. Dogo, S. U. Michael, F. O. Uloko and A. O. Salawu, *East Eur. J. Phys.*, 2021, **2021**, 5–17.
- 70 X. Qiu, Y. Jiang, H. Zhang, Z. Qiu, S. Yuan, P. Wang and B. Cao, *Phys. Status Solidi RRL*, 2016, **10**, 587–591.
- 71 H. Pujiarti, R. Hidayat and P. Wulandari, *Key Eng. Mater.*, 2020, **860**, 22–27.
- 72 A. Kaltzoglou, M. Antoniadou, A. G. Kontos, C. C. Stoumpos, D. Perganti, E. Siranidi, V. Raptis, K. Trohidou, V. Psycharis, M. G. Kanatzidis and P. Falaras, *J. Phys. Chem. C*, 2016, **120**, 11777–11785.
- 73 I. Chabri, Y. Benhouria, A. Oubelkacem, A. Kaiba, I. Essaoudi and A. Ainane, *J. Electron. Mater.*, 2023, **52**, 2722–2736.
- 74 D. Pal, *Adv. Theory Simul.*, 2023, **6**, 2200856.

